Solute exchange through gap junctions lessens the adverse effects of inactivating mutations in metabolite-handling genes

Stefania MONTERISI[1], Johanna MICHL[1], Alzbeta HULIKOVA[1], Jana KOTH[2], Esther M. BRIDGES[3], Amaryllis E. HILL[1], Gulnar ABDULLAYEVA[2], Walter F. BODMER[2], Pawel SWIETACH[1]*

[1]Department of Physiology, Anatomy & Genetics, Oxford, Parks Road, OX1 3PT, UK

[2]MRC Weatherall Institute for Molecular Medicine, John Radcliffe Hospital, Oxford OX3 9DS, UK

[3]Department of NDM Experimental Medicine, MRC Human Immunology Unit, MRC Weatherall Institute of Molecular Medicine, JR Hospital, Oxford, OX3 9DS, UK

*Address for correspondence: Professor Pawel Swietach, Department of Physiology, Anatomy and Genetics, Parks Road, Oxford OX1 3PT, UK. Email: pawel.swietach@dpag.ox.ac.uk

KEYWORDS: metabolism; diffusion; oxidative phosphorylation; Warburg; pH homeostasis; variation; carcinogenesis.

Authors declare no conflicts of interest

ABSTRACT

Growth of cancer cells *in vitro* can be attenuated by genetically inactivating selected metabolic pathways. However, loss-of-function mutations in metabolic pathways are not negatively selected in human cancers, indicating that these genes are not essential *in vivo*. We hypothesize that spontaneous mutations in 'metabolic genes' will not necessarily produce functional defects because mutation-bearing cells may be rescued by metabolite exchange with neighboring wild-type cells via gap junctions. Using fluorescent substances to probe inter-cellular diffusion, we show that colorectal cancer (CRC) cells are coupled by gap junctions assembled from connexins, particularly Cx26. Cells with genetically inactivated components of pH regulation (*SLC9A1*), glycolysis (*ALDOA*), or mitochondrial respiration (*NDUFS1*) could be rescued through access to functional proteins in co-cultured wild-type cells. The effect of diffusive coupling was also observed in co-culture xenografts. Rescue was largely dependent on solute exchange via Cx26 channels, a uniformly and constitutively expressed isoform in CRCs. Due to diffusive coupling, the emergent phenotype is less heterogenous than its genotype, and thus an individual cell should not be considered as the unit under selection, at least for metabolite-handling processes. Our findings can explain why certain loss-of-function mutations in genes ascribed as 'essential' do not influence the growth of human cancers.

INTRODUCTION

The role of somatic evolution in advancing cancers is well-established (1,2) and can be modelled mathematically (3,4). Its central paradigm asserts that mutations benefiting cancer cells undergo positive selection and appear enriched in cancers. Cells carrying 'advantageous' genetic changes may evade the normal checks and controls that restrict proliferation (5), or become resistant to harsh microenvironments found in tumors (6). Conversely, mutations that inactivate critically-important processes are predicted to emerge less frequently than the random mutation rate as a result of negative selection (7). Multiple *in vitro* knockout screens have identified genes deemed essential for cell survival (8,9), among which are genes involved in metabolic pathways (10,11). Loss-of-function mutations in these processes are predicted to undergo negative selection in human cancers (12,13), but this phenomenon is exceedingly rare *in vivo*, equating to only tens of genes (14) such as those involved in protein synthesis and immune-exposed epitopes, but not metabolite handling (12). The reason for the discrepancy between the interpretation of *in vitro* screens and *in vivo* observations remains unclear, but highlights fundamental differences in gene essentiality under culture conditions and in human tumors. We hypothesize that inactivating mutations in key metabolic pathways may be rescued by access to operational proteins in neighboring wild-type cells, a scenario more likely in tumors bearing spontaneous mutations compared to mutagenized mono-cultures *in vitro*. Thanks to this rescue effect, the aforementioned mutations will not incur a functional deficit to the mutation-bearing cell which, in turn, will not undergo negative selection. A plausible means of rescue could involve connexin-assembled gap junctions that allow metabolite exchange between cells across the continuous cytoplasmic space, or syncytium (15-18).

Indeed, early work on gap junctions in fibroblasts provided evidence for metabolic cooperation, whereby connected cells can compensate for complementary deficiencies, such as enzymic activity (19-21). However, the prevailing paradigm at the time stated that cancer cells do not form gap junctions (22), and thus cannot benefit from metabolic cooperation. The prominence of gap junctions in cancer has since been revised (15-18), but the feasibility of metabolic rescue remains to be tested. In the proposed model, an inactivating mutation arising spontaneously within a coupled network of cancer cells may not emerge as deleterious when the affected cell can access metabolite-handling enzymes or transporters in neighboring cells across connexin-assembled channels. If, however, the same mutation is introduced experimentally in all cells (as is common with *in vitro* assays), diffusive exchange is unable to restore metabolic function, irrespective of coupling strength. We speculate that the diffusive exchange of metabolites via gap junctions may explain why some metabolic processes, deemed to be essential for survival *in vitro*, do not undergo negative selection in cancers. This model shares similarity to the bystander effect, whereby toxins or therapeutic agents can spread across a tumor via gap junctions (17,23-26). Metabolic rescue of gene mutations would add another dimension to the role of gap junctions in cancer by addressing their longer-term consequences on carcinogenesis, and offering an explanation for the scarcity of negatively selected genes.

This study used colorectal cancer (CRC) cells to test our hypothesis that diffusive exchange can rescue cells carrying inactivating mutations in apparently critical genes. We first assessed the degree of cell-to-cell coupling in a panel of CRC cells and identified the major connexin isoforms responsible for assembling these conduits. We then genetically inactivated metabolic processes that play

important roles in cancer, to test whether coupling onto wild-type cells can compensate the functional deficit. The inactivated functions included *(i)* Na^+/H^+ exchanger-1 (*SLC9A1*), a pH regulator at the plasma membrane that is critical for survival under acidic conditions (27); *(ii)* aldolase A (*ALDOA*), a glycolytic enzyme that is critical for the Warburg effect (28); *(iii)* NADH:ubiquinone oxidoreductase core subunit S1 (*NDUFS1*), part of complex I required for oxidative phosphorylation (29). In support of our hypothesis, we found that co-culturing genetically modified cells with wild-type counterparts rescues the functional deficit by allowing access to operational proteins in neighboring cells. Moreover, we confirm this rescue effect in xenografts *in vivo*. Based on our findings, we propose that connexin-dependent metabolite exchange lessens the deleterious effects of mutations in genes related to metabolism.

RESULTS

Screening colorectal cancer cells for connexin expression

Microarray data from seventy-nine CRC lines (30) were analyzed for the expression of connexin (Cx) genes. Expression in a subset of CRC cells was detected for *GJA1* (coding for Cx43), *GJA3* (Cx46), *GJB1* (Cx32), *GJB2* (Cx26), *GJB3* (Cx31), *GJB5* (Cx31.1) and *GJC1* (Cx45) (**Figure 1A)**. Gaussian mixture modeling (GMM) determined that the distributions of *GJA1, GJA3, GJB1, GJB5* and *GJC1* message among CRC lines were bimodal, such that cell lines could be grouped as high- or low-expressing. In contrast, messages for *GJB2* and *GJB3* were unimodally distributed among the cell lines. Analysis of TCGA datasets confirmed bimodality for *GJA3*, *GJB5* and *GJC1* expression (**Figure 1-figure**

supplement 1). Single-cell transcriptomics (31) indicated expression of *GJB1*, *GJB2* and *GJB3* in normal colonic epithelial cells (**Figure 1B**). *GJB2* and *GJB3* had previously been identified in normal colorectal epithelium (32,33). Thus, *GJB2* and *GJB3* are constitutively expressed in CRC cell lines, whereas *GJA1*, *GJA3* or *GJC3* were found in a subset of lines, presumably due to mutations or stable methylation differences in their promoter regions. Two-by-two table analysis for bimodally-distributed connexin genes indicated positive correlations between *GJA1* and *GJC1*, and negative correlations for pairs *GJB1*-*GJA1*, *GJB1*-*GJB5* and *GJB1*-*GJC1* (**Figure 1C;** see also principal component analysis **Figure 1-figure supplement 2**).

Figure 1D shows the expression of connexin genes, ranked by combined *GJB2* and *GJB3* message. Fourteen lines were selected for further functional measurements (**Figure 1E**). Since *GJA1* expression accounted for considerable variation, cell lines were categorized as *GJA1*-high and *GJA1*-low. The *GJA1*-low group could be subdivided further as *GJC1*-low and *GJC1*-high. This classification was confirmed at protein level using antibodies against Cx43 (*GJA1*) (**Figure 1F**). RKO cells were chosen as a negative control because of negligible expression of major Cx genes.

Cx26 (GJB2) channels are a major route for diffusive exchange in CRC cells

Solute diffusion between cells was measured by FRAP (fluorescence recovery after photobleaching) of fluorescent calcein (34). A cell in the middle of a coupled cluster was bleached to ~50% of resting signal, and the subsequent recovery of fluorescence, due to dye ingress from neighboring cells, indicated the degree of coupling. Fluorescence recovery was detected in *GJB2*-expressing

SNU1235 but not in RKO cells (**Figure 2A**). FRAP recordings were quantified in terms of an apparent permeability constant for calcein (**Figure 2B**), and the role of Cxs was confirmed from the inhibitory effect of carbenoxolone (100 μM), a broad-spectrum Cx blocker (**Figure 2C**). The acquired images supply data on cell geometry and time courses of calcein fluorescence for estimating permeability to calcein, albeit with assumptions detailed in Appendix 1. Cell-to-cell calcein permeability correlated best with *GJB2* expression (**Supplementary File 1**). *GJB2* knockdown ablated functional coupling, whereas siRNA against *GJB3* did not (**Figure 2D**; see **Figure 2-figure supplement 1** for knockdown confirmation). In *GJA1*-high CACO2 cells, functional coupling was ablated with siRNA against *GJA1* (**Figure 2E;** see **Figure 2-figure supplement 2** for knockdown confirmation). Note, that there was a trend for *GJB3* knockdown to increase overall connectivity in DLD1 and SNU1235 cells, which may represent compensatory changes in the expression of other connexins or the intimacy of cell-cell contacts. Western blot analysis indicated some degree of interaction between the expression of particular pairs of connexins, but the effects were, at best, modest (**Figure 2-figure supplement 1**).

Functional estimates of coupling correlated well with levels of Cx26 protein at cell-to-cell contacts (**Figure 2F**). Furthermore, Cx43 was detected at cell-to-cell contacts in C10, LOVO and CACO2 but not in RKO, SW1222 or HT29 cells (**Figure 2G**). Unlike Cx26 staining, which was fairly uniform among cells, Cx43 immunofluorescence appeared more heterogenous, with only some cells in a monolayer appearing strongly positive. To confirm the co-existence of Cx43-positive and negative populations, LOVO and Caco2 were FAC-sorted by Cx43 status, expanded, and analyzed by western blot. This analysis identified distinct Cx43-

positive and negative populations, indicating that not all cells of a nominally *GJA1*-positive line may benefit from Cx43-dependent connectivity (**Figure 2H**).

Ablation of *GJB2* expression by guide RNA (gRNA) or siRNA (**Figure 2I**) eliminated Cx26 immunofluorescence (**Figure 2J**). *GJB2* knockout (KO) clones of DLD1 cells, generated by CRISPR/Cas9 (**Figure 2K**), had dramatically reduced diffusive exchange (**Figure 2L**). *GJB2* knockdown did not affect Cx31 or Cx43 expression patterns in DLD1 cells (**Figure 2-figure supplement 1**), arguing against any compensatory transcriptional changes. In summary, Cx26 channels provide a principal route for cell-to-cell communication in most CRC lines, and the level of this protein is expressed relatively uniformly among cells.

Small cytoplasmic molecules equilibrate across coupled CRC monolayers

FRAP-based measurements can identify the Cx channels that underpin permeability but cannot predict the extent to which solutes equilibrate at steady-state. The latter was evaluated from the degree of fluorescent dye exchange in co-cultures prepared from two populations of cells loaded with spectrally distinct CellTracker fluorophores. The diffusive properties of CellTracker dyes, determined by FRAP (**Figure 3A**), correlated inversely with molecular weight (**Figure 3B**). CellTracker Violet and Orange were selected for co-culture experiments (**Figure 3C**). Monolayers were imaged sequentially for Violet or Orange in confocal mode. In control monolayers prepared with one dye only, fluorescence bleed-through between channels was minimal (**Figure 3D**). CellTracker Violet and Orange fluorescence images were pseudo-colored as blue and red respectively, such that pixels containing both dyes (i.e. diffusive exchange) would appear purple (**Figure 3D**). In

188 eight CRC lines, selected to span a range of *GJB2* expression, dye exchange was
189 confirmed, particularly in areas of high cell confluency (**Figure 3E**), pointing to the
190 role of cell-to-cell contacts in exchange. As confirmation that dye-mixing was due to
191 exchange across cell-to-cell contacts, co-culture experiments were repeated on cells
192 seeded at very low density, which reduces the incidence of cell-to-cell contacts and
193 yields less exchange (**Figure 3F**). Furthermore, negative control RKO co-cultures did
194 not show evidence for significant mixing between cells (**Figure 3F**).

195 The degree of dye mixing arising from cell-to-cell exchange was quantified in
196 terms of a coupling coefficient. This coefficient compares fluorescence emitted from
197 each of the two CellTracker dyes as a fraction of total fluorescence, and reports the
198 lower of these two numbers (see Supplemental Method for details). Thus, before
199 dye exchange takes place, the coupling coefficient is zero; if dye exchange can take
200 place across gap junctions, this coefficient increases as pixels become dually
201 fluorescent. In monocultures, the coupling coefficient was negligible, as expected
202 from a control experiment in which only one dye is present (**Figure 3-figure**
203 **supplement 1**). In contrast, co-cultures produced significant coupling coefficients for
204 cells expressing functional gap junctions, seeded at adequate density that favors
205 close cell-cell contacts (**Figure 3G**). Negative control RKO cells, DLD1 *GJB2* KO
206 cells, or DLD1 and OXCO1 cells plated at low density produced low coupling
207 coefficients. Strikingly, there was no correlation between FRAP-measured
208 permeability to calcein and coupling coefficient determined at steady-state for cell
209 tracker dyes. Thus, even monolayers with low-conductance gap junctions can
210 produce a uniform distribution of diffusible substances at steady-state. Coupling
211 coefficients showed considerable heterogeneity when plotted as a frequency
212 distribution, with least coupling in RKO cells and low-density DLD1 and OXCO1

monolayers (**Figure 3H**). In the remaining cell lines tested, around half of the cells showed evidence for significant coupling. This number is likely to under-estimate the extent of coupling in tissues, where contacts are established in three dimensions.

Some degree of dye leakage from cells is inevitable during long-term culture, but this is unlikely to result in the transfer of dye into neighboring cells. Firstly, CellTracker dyes are chemically rendered to be membrane-impermeable inside cytoplasm, thus any molecules that leak across damaged membranes cannot (re)enter neighboring cells. Secondly, the volume of extracellular space is far greater than the intracellular volume, thus any released dye would become vanishingly diluted outside cells. For these reasons, the dye exchange measurements report the consequences of cell-to-cell diffusion across gap junctions, rather than transfer across the extracellular milieu.

Dye exchange was tested further using flow cytometry (**Figure 4A**). Co-cultures were prepared using various pairs of spectrally-resolvable CellTracker dyes. The gain of detection channels was calibrated using mono-cultures prepared using one dye only. After gating-out duplets, fluorescence was measured on two detection channels. DLD1 cells grown as mono-cultures emitted fluorescence detected on one channel only (**Figure 4B**). Co-cultures, in contrast, produced a cluster of cells emitting fluorescence in both channels, indicating that dye exchange had occurred during culture. This can be visualized by overlaying pseudo-colored density histograms for co-cultures (as green) against the two mono-cultures (as red or blue). To confirm that dye exchange had taken place whilst cells were connected as part of an intact monolayer, control experiments mixed two suspensions of cells harvested from distinctly labelled mono-cultures immediately prior to cytometry (i.e. without a period of culture when cells are coupled to one another). These experiments

produced two separate clusters (**Figure 4C**), confirming that dual labelling arises only in intact co-cultures. Similar experiments were performed in other CRC cells (**Figure 4D-G**). The extent of dye exchange between coupled cells was calculated to be ~60% (DLD1 or HT29 cells; **Figure 4H**).

In summary, coupled CRC cells can freely exchange solutes under 1 kDa across connexin channels, thus small metabolites are expected to equilibrate across the continuous cytoplasmic compartment. The next series of experiments sought evidence that diffusive exchange can functionally rescue cells carrying a genetic inactivation of a specific metabolite-handling process. .

Coupling rescues genetically inactivated trans-membrane Na^+/H^+ exchange

The Na^+/H^+ exchanger NHE1, coded by *SLC9A1*, is a prominent regulator of intracellular pH (pHi), expressed in many CRC cells including HCT116. Genetic inactivation of NHE1 affects pHi control and is detrimental to cellular physiology (35). If gap junctions were able to conduct a sufficient flow of H^+ ions between coupled cells, then it is conceivable for an *SLC9A1*-deficient cell to have its pHi-regulatory needs serviced by a neighboring wild-type cell. To test this, two *SLC9A1* KO clones were generated using CRISPR/Cas9 (**Figure 5A**). Confirmation that these KO cells lack NHE1 activity was sought in monolayers loaded with the pH-reporter dye cSNARF1. In wild-type (WT) HCT116 cells, NHE1 activity was measured from the rate of pHi recovery following an acid-load (ammonium prepulse) in the absence of CO_2/HCO_3^- to eliminate HCO_3^- dependent transporters. NHE1 activity was confirmed from the inhibitory effect of cariporide (**Figure 5B**). KO monocultures, in contrast, produced no cariporide-sensitive pHi recovery. To test if pHi regulation in KO cells

262 could be rescued by coupling onto WT cells, co-cultures were established, wherein
263 KO cells were identified by transfected GFP fluorescence (**Figure 5C**). pHi recovery,
264 following an ammonium prepulse, was tracked simultaneously in WT and KO cells
265 (**Figure 5D**). Strikingly, KO cells showed evidence for pHi recovery when co-cultured
266 with WT neighbors, despite the absence of *SLC9A1* expression. WT cells in co-
267 culture produced slower pHi recoveries than in monocultures because of the
268 additional burden of having to service KO cells. Similar observations were made with
269 either KO clone. These experiments illustrate phenotypic blurring: apparent function
270 is more homogenous than the underlying genotype.

271 To test how diffusive exchange impacts on steady-state pHi, measurements
272 were performed on cells equilibrated in HEPES/MES-buffered medium over a range
273 of extracellular pH (pHe). In WT cells, the pHe-pHi relationship was linear and not
274 affected by knockout of *GJB2* (**Figure 5E**). Steady-state pHi was reduced in KO
275 monocultures, as expected from impaired pHi control. However, the pHi difference
276 between WT and KO cells collapsed in co-cultures. This effect was Cx26-dependent
277 because *SLC9A1*-expressing HCT116 cells that had genetically inactivated *GJB2*
278 were unable to raise the pHi of co-cultured KO cells (**Figure 5E**). Since the readout
279 of pHi regulation can be recorded with single-cell resolution, the distribution of pHi
280 among cells was analyzed to seek an effect of coupling on cell-to-cell variation.
281 *SLC9A1*-deficient cells have weaker pHi control, which manifests as a wider pHi
282 distribution in mono-cultures (**Figure 5F**). When, however, these knockout cells
283 were co-cultured with WT cells, the pHi distribution returned to normal levels. This
284 observation indicates that NHE1 activity in WT cells was able to service the pHi-
285 regulatory needs of KO cells, manifesting as a narrowing of the population-wide

spread of pHi. This rescue effect was Cx26-dependent because knockdown of *GJB2* resulted in a wider pHi spread (**Figure 5F**).

To test if diffusive exchange benefits the growth of *SLC9A1*-deficient cells, co-cultures were established from different seeding ratios of WT and KO cells. Parallel plates were set-up to record growth at various time points. Total biomass (i.e. growth of WT and KO cells) was measured by the sulforhodamine B (SRB) absorbance assay and growth of the KO compartment was determined from GFP fluorescence. In the case of KO monocultures, the GFP and SRB signals measure an equivalent quantity and therefore provide a calibration curve for converting between the two measurements. This calibration curve allows a measured SRB signal to be converted into an expected GFP signal for co-culture experiments, and thereby seek evidence for any enrichment due to metabolic rescue. If WT and KO cells had indistinguishable survival prospects, then the time courses of GFP and SRB should be stoichiometrically related to the seeding ratio, i.e. measured GFP should equal SRB scaled by the seeding density (e.g. by 50% for a 1:1 co-culture). If, however, there is a growth advantage for KO cells in the presence of WT cells, then measured GFP will exceed that predicted from SRB. To test for such rescue, co-cultures were established over a range of seeding ratios. Experiments were performed in media at pH 7.4 or 6.6 to stimulate NHE1 over a range of pH. For co-cultures seeded from 25% KO or 50% KO cells, growth of the GFP-tagged KO compartment exceeded the prediction based on equal WT/KO survival (**Figure 5G/H**). Similar findings were observed using the second KO line (**Figure 5-figure supplement 1**). Thus, co-cultured *SLC9A1*-deficient cells grew faster than expected at the expense of coupled WT cells. Since pHi regulation consumes a substantial amount of energy, this effect could be explained by the exploitation of WT resources by KO cells.

In summary, we show that cells lacking an important ion exchanger at the membrane can hijack the equivalent activity from neighboring wild-type cells, provided that the ions are able to diffuse across connexin channels.

Coupling rescues genetically inactivated glycolytic metabolism

The next test related to glycolysis, a critical metabolic pathway that handles small molecules in cytoplasm. DLD1 cells were selected for these experiments based on their high glycolytic rate. A recent whole-genome CRISPR-Cas9 screen identified *ALDOA*, a gene coding for the glycolytic enzyme aldolase A, as essential for CRC cell survival under physiological pH (36). Ablation of *ALDOA* using virally transduced gRNAs reduced the expression (**Figure 6A**) and glycolytic rate, assayed in terms of medium acidification (**Figure 6B**) and lactate production (**Figure 6C**). It was not possible to produce a stable *ALDOA* knockout clone, ostensibly because of the enzyme's critical role for survival, thus experiments were performed within 6 days after transduction with one of the two gRNA constructs.

ALDOA-deficient DLD1 cells grew four-times slower than wild-type cells (**Figure 6-figure supplement 1**), ostensibly due to compromised provision of glycolytic ATP and build-up of fructose-1,6-bisphosphate, the substrate for aldolase A. These metabolites are expected to diffuse freely between coupled cells, thus any fructose-1,6-bisphosphate that accumulates in an *ALDOA*-deficient cell should diffuse to neighboring cells for processing, whereas ATP will diffuse in the opposite direction. Diffusive rescue would allow *ALDOA*-deficient cells in co-culture with wild-type cells to grow faster than expected. To test this, co-culture experiments were performed for various ratios of WT and GFP-labelled *ALDOA*-deficient cells (**Figure**

335 **6D**). After 6 days of culture at pH 7.4, GFP fluorescence (a measure of *ALDOA*-
336 deficient cells) and SRB absorbance (total cell biomass) were recorded. If *ALDOA*-
337 deficient cells received no benefit from being coupled onto WT cells, then the end-
338 point GFP signal would be proportional to the initial seeding density (**Figure 6E;** grey
339 line). However, GFP-labelled cells became relatively enriched in co-cultures with WT
340 cells, which was most prominent at 3:1 seeding ratio. Thus, the survival of *ALDOA*-
341 deficient cells improved when these connected onto WT counterparts . A similar
342 effect was seen using the other gRNA (**Figure 6F**). Rescue of *ALDOA*-deficient cells
343 in co-culture with WT cells was absent when *GJB2* was knocked-out in WT cells with
344 gRNA (**Figure 6G**), indicating a critical role for Cx26-mediated metabolite exchange
345 in this rescue. As a negative control, co-culturing *ALDOA*-deficient DLD1 cells with
346 wild-type RKO cells, a line that does not support connexin connectivity, failed to
347 rescue *ALDOA*-deficient cells (**Figure 6-figure supplement 2**).

348 To test if connexin isoforms other than Cx26 are able to support metabolic
349 rescue, experiments were performed on two *GJB2*-low cell lines: C10 and NCIH747.
350 C10 cells express Cx43 channels, which produce good cell-to-cell coupling, albeit in
351 a sub-population of cells due to its heterogeneous expression pattern (see **Figure**
352 **2G**). Co-culturing of *ALDOA*-deficient C10 cells with wild-type counterparts did not
353 result in significant metabolic rescue (**Figure 6H;** see **Figure 6-figure supplement 3**
354 for knockdown confirmation). This may relate to Cx43 heterogeneity, which allows
355 only Cx43-positive cells to benefit from metabolic rescue. NCIH747 cells express
356 both Cx31 and Cx45 but neither were unable to rescue *ALDOA*-deficient cells in co-
357 culture with wild-type cells (**Figure 6I;** see **Figure 6-figure supplement 3** for
358 knockdown confirmation).

In summary, we demonstrate that the genetic ablation of a metabolite-handling cytoplasmic enzyme in one cell can be rescued by diffusive access to the required catalysis in neighboring cells via connexin channels. Thus, despite major differences in genotype, the apparent phenotype of KO and WT cells is more similar. Cx26-assembled channels emerge as particularly effective in supporting metabolic rescue.

Coupling rescues genetically inactivated mitochondrial respiration **in vitro**

The third test for metabolite exchange used cells with genetically inactivated mitochondrial respiration on the basis that this organellar process influences the levels of diffusible substances in cytoplasm, including ATP. SW1222 cells were selected on the basis of their high respiratory rate (**Figure 7B**), which could be genetically inactivated by knockout of *NDUFS1*, a gene coding for a component of complex I (**Figure 7A**) (36). Oxidative phosphorylation was blocked in *NDUFS1* KO cells, and a compensatory increase in glycolytic rate ensued (**Figure 7B**). *NDUFS1*-deficient cells grew three times slower than WT cells (**Figure 7-figure supplement 1**), likely due to ablated mitochondrial metabolism that is critical for delivering substrates and energy. To test if junctional coupling could rescue *NDUFS1*-deficient cells, WT and GFP-labelled KO cells were co-cultured in medium at pH 7.7 (alkaline conditions that activate glycolysis fully; **Figure 7C**). If KO cells received no benefit from being coupled onto WT cells, the end-point GFP signal would be proportional to the seeding ratio. However, co-culture with WT cells promoted the growth of GFP-labelled KO cells beyond the expected level, particularly for seeding ratios of 3:1 KO:WT (**Figure 7D**). This rescue related to the density of cell-to-cell contacts,

because KO cells could no longer receive a growth benefit in sparse co-culture with WT cells (**Figure 7E**). Furthermore, the rescue was linked to Cx26-dependent coupling as co-culture with WT cells that had genetically knocked-down *GJB2* by siRNA yielded no benefit to co-cultured *NDUFS1*-deficient cells (**Figure 7F**). Ultimately, the rescue effect of WT cells relates to oxidative phosphorylation, which requires oxygen and should be lessened under hypoxic conditions. Indeed, this was the case in co-cultures incubated in 2% O_2 (**Figure 7G**).

The importance of Cx26-assembled channels in providing metabolic rescue to *NDUFS1* KO cells was tested in co-cultures with *GJB2*-low/negative lines: RKO, C10, and NCIH747 (**Figure 7H**). RKO cells, which do not express connexin genes, were unable to rescue *NDUFS1*-deficient SW1222 cells. *GJA1*-positive C10 cells, which form Cx43-dependent connections, did not rescue *NDUFS1*-deficient cells, which indicates that Cx26 and Cx43 channels are unlikely to form heterotypic channels, in agreement with previous findings (37). . Finally, NCIH747 which produce Cx31 and Cx45 also did not rescue *NDUFS1*-deficient cells, further supporting the notion that heterotypic channels are less efficacious than Cx26-assembled conduits.

Cx26 coupling rescues genetically inactivated mitochondrial respiration **in vivo**

Whilst *in vitro* assays provide a well-controlled environment for evaluating metabolic rescue, their findings must be verified *in vivo*, wherein cells are able to connect extensively in three dimensions and allowed to grow over many cycles of division. Evidence for connexin-dependent metabolic rescue *in vivo* was tested in

xenografts seeded from a 1:1 mixture of GFP-labelled *NDUFS1*-deficient (KO) SW1222 cells and DLD1 cells. In this system, DLD1 cells lay down a matrix for *NDFUS1* KO cells to grow in, and metabolic rescue by respiring DLD1 cells would promote the growth of the mitochondrially-defective (GFP-positive) cellular population. Xenografts of wild-type DLD1 plus *NDUFS1* KO SW1222 cells were established subcutaneously on the left flank of mice. As a control, the opposite flank of the mouse was injected with a mixture of *NDUFS1* KO SW1222 cells plus Cx26-deficient (*GJB2* knockout) DLD1 cells (**Figure 8A**), i.e. a combination that cannot establish significant strong DLD1-SW1222 coupling. In DLD1 cells, genetic inactivation of *GJB2* had no substantial effect on cell growth (**Figure 8B**) or ability to form 3-D spheroids (**Figure 8C**), thus both types of DLD1 cells were deemed suitable for growing xenografts.

In terms of bulk volume, xenografts grew faster on the left flank, i.e. where DLD1 and SW1222 cells can establish Cx26-assembled gap junctions (**Figure 8D**). At the end-point (combined left and right tumor burden >1 cm^3 or 30 days of growth), xenografts were excised for histology and stained with the nuclear dye Hoechst and GFP antibody to enhance visualization of GFP-tagged *NDUFS1*-deficient cells (**Figure 8E**). GFP-positive cells were identified by an image analysis pipeline (see Methods) that quantifies the number of clusters and their combined area, repeated across the tumor height. This analysis confirmed larger tumors on the left flank, containing more GFP-positive clusters and a larger combined GFP-positive area (**Figure 8F**). These inferences were unaltered by changing the threshold for defining GFP-positive areas (**Figure 8-figure supplement 1**). Overall, these *in vivo* findings confirm that DLD1 cells are able to rescue *NDUFS1*-deficient SW1222 cells in a Cx26-dependent manner, consistent with *in vitro* co-culture observations.

In summary, we show that genetically inactivated mitochondrial metabolism in one cell can be rescued by coupling onto a wild-type cell *in vivo* and *in vitro*. This demonstrates that apparent differences in phenotype can be reduced by diffusive coupling, even if the inactivated process occurs in a subcellular compartment (**Figure 8G/H**).

DISCUSSION

The results of this study show that CRC cells establish a multi-cellular cytoplasmic continuum through which small molecules are able to diffuse and equilibrate. Solute exchange was demonstrated using fluorescent dyes in terms of an apparent permeability constant and degree of mixing at steady-state. The apparent permeability to calcein, as measured by FRAP, varied among CRC cell lines, and correlated best with *GJB2* expression and Cx26 immunoreactivity at cell-to-cell contacts. The role of this particular connexin isoform in producing functional conduits was inferred from the effect of genetic knockdown on permeability, which was most sensitive to siRNA against *GJB2*. The gene coding for Cx26 is expressed in normal colorectal epithelium (38), and the unimodal distribution of its message level among CRC lines suggests that transformed cells retain its expression, with a few notable exceptions (e.g. RKO). In addition to *GJB2*, some CRC cells express isoforms such as *GJA1* and *GJC1*, possibly due to mutations or stable epigenetic changes present only in a subset of CRC lines. Intriguingly, the magnitude of calcein permeability measured by FRAP did not predict the degree to which solutes equilibrate between cells at steady-state, as measured by coupling coefficient. This is because even weakly coupled confluent monolayers can exchange dyes, if allowed sufficient time. Thus, the phenomenon of solute equilibration across coupled cellular networks is likely to be significant even in cancer cells with nominally low connexin expression.

In the context of cancer, diffusion through connexin-assembled channels is significant for growth when it includes important metabolites handled by enzymes or transporters that are susceptible to genetic mutations. In the event of a loss-of-function mutation, the absence of activity could be compensated by access to

463 operational proteins in neighboring cells, potentially over a few cell lengths only
464 (**Figure 8G/H**). This rescue effect was confirmed for three cases of biologically
465 important processes that handle small molecules at distinct sub-cellular domains: at
466 the plasma membrane (NHE1, coded by *SLC9A1*, handling intracellular H^+ ions), in
467 the cytoplasm (aldolase A, coded by *ALDOA*, handling the glycolytic intermediate
468 fructose-1,6-bisphosphate) and in mitochondria (NADH:ubiquinone oxidoreductase
469 core subunit S1; *NDUFS1*, part of complex I). Monocultures of genetically-altered
470 cells manifested a functional defect, namely, impaired pHi regulation (*SLC9A1*-
471 deficient cells), blocked glycolysis (*ALDOA*-deficient cells) or inactivated
472 mitochondrial respiration (*NDUFS1*-deficient cells). However, co-culture with wild-
473 type counterparts provided rescue, detected as an enrichment in cells carrying the
474 genetic ablation. Metabolic rescue by connexins was observed *in vitro*, as well as *in*
475 *vivo*, where it allowed a genetically defective cell (*NDFUS1* KO) to expand faster
476 than otherwise. The rescue effect was related to Cx26 channels because it became
477 ablated by genetically inactivating *GJB2*. However, a role for other connexin
478 isoforms cannot be excluded, although the present findings indicate that Cx26-
479 low/negative cells expressing *GJB3* (Cx31) or *GJA1* (Cx43) were unable to match
480 the metabolic rescue provided by Cx26 pathways. In the case of Cx31, the
481 conductance established by these channels is likely to be small, as its knockdown
482 did not reduce ensemble permeability. Strong conductances could be established in
483 Cx43-positive cells, but these tended to be heterogenous within a monolayer,
484 restricting the benefit of metabolic rescue to only a subset of cells. This pattern of
485 expression may explain why Cx43 is less efficacious in metabolic rescue compared
486 to the more uniformly distributed Cx26.

Metabolic rescue by gap junctions is relevant to our understanding of somatic evolution in cancer because it provides a mechanism by which cells carrying loss-of-function mutations in metabolite-handling genes are able to survive and divide, as long as connections are made onto wild-type neighbors (**Figure 8G/H**). Consequently, cells acquiring such spontaneous mutations will evade negative selection in a human tumor. However, the same mutation studied in a monoculture may be lethal because this *in vitro* setting does not offer a means of rescue from wild-type cells. Metabolic rescue by gap junctions may explain why some genes are found to be essential *in vitro*, but not *in vivo* (i.e. their inactivating mutations are not negatively selected). In contrast, genes responsible for processes that do not handle diffusible solutes cannot benefit from connexin-mediated coupling, irrespective of their cellular neighborhood. This category include genes coding for ribosomal subunits that are too large to cross connexin channels or for neoantigens that are, by design, confined to the mutation-carrying cell. Inactivating mutations in such genes may be selected negatively as there are no tangible ways for compensating the ensuing functional deficit (12).

A secondary implication of our findings in the context of carcinogenesis relates to the definition of the unit that is being selected during somatic evolution. A key assumption of current tumorigenesis models is that mutations act in a cell-autonomous fashion. Exceptions to this paradigm have been postulated for autocrine interactions (39), but the role of gap junctional connectivity has not been explored. In terms of genotype, each cell in a tumor is a distinct unit, responding independently to selection pressures. However, diffusive coupling between cells of contrasting genotype can produce an emergent phenotype that is less distinct. This scenario can arise in the case of spontaneous mutations affecting metabolite-handling genes, and

512 is significant because the coupled cells will have comparable survival prospects,
513 despite striking differences in genotype. In this system, the unit under selection
514 extends beyond a single cell. Our findings emphasize the importance of measuring
515 phenotypic variation, particularly in instances relating to diffusible molecules, as this
516 may not overlay with the more compartmentalized genotypic landscape. In cases
517 where phenotypic differences are reduced as a result of connexin connectivity, it is
518 not appropriate to consider a single cell as the unit under selection (40). Intriguingly,
519 connexin genes are rarely mutated in cancer (12). We speculate that this reflects a
520 critical role of conductive cell-to-cell coupling for cancer growth, and presents an
521 opportunity for therapeutic interventions.

MATERIALS AND METHODS

Key resource table.

Reagent type (species) or resource	Designation	Source or reference	Identifiers	Additional information
Chemical compound	anti-adherence rinsing solution	Stemcell Technologies	07010	
Chemical compound	SULPHORODAMINE for SRB Assay	Sigma-Aldrich	3520-42-1	
Chemical compound/drug	cSNARF1	Thermo Fisher	C1271	
antibody	Anti Cx31 (mouse monoclonal)	Proteintech	12880-1-AP	1:1000
antibody	Anti Cx26 (mouse monoclonal)	Invitrogen	CX-1E8	1:1000
antibody	Anti Cx43 (rabbit polyclonal)	Thermo Fisher	13-8300	1:1000
antibody	Anti GAPDH (mouse monoclonal)	Proteintech	HRP-60004	1:6000
antibody	Anti beta actin (mouse monoclonal)	Proteintech	HRP-60008	1:6000

antibody	Anti Cx43 APC-conjugated (mouse monoclonal)	R&D Systems	FAB7737A	1:500
antibody	Anti NDUFS1 (rabbit polyclonal)	ThermoFisher	PA5-22309	1:3000
antibody	Anti Aldolase A (rabbit polyclonal)	Novus Biologicals	NBP1-87488	1:3000
antibody	Anti GFP (rabbit polyclonal)	ThermoFisher	A-11122	1:1000
Chemical compound/drug	Cariporide	Tocris	5358	
Chemical compound/drug	Lipofectamine RNAiMAX	Invitrogen	2373383	
sequenced-based reagent	siRNA	Dharmacon	siGENOME SMARTpool M-011042-01-0005	Silencer Select
sequenced-based reagent	siRNA	Dharmacon	siGENOME SMARTpool L-019285-00-0005	Silencer Select
sequenced-based reagent	siRNA	Dharmacon	siGENOME SMARTpool M-019948-02-0005	Silencer Select
sequenced-based reagent	siRNA	Dharmacon	siGENOME NONtargeting control D-001210-01-05	Silencer Select
Chemical compound	Cell Tracker fluorescent dye violet	Invitrogen	C10094	

Chemical compound	Cell Tracker fluorescent dye orange	Invitrogen	C34551	
Chemical compound	Cell Tracker fluorescent dye green	Invitrogen	C2925	
Chemical compound	Cell Tracker fluorescent dye deep red	Invitrogen	34565	
sequence-based reagent	LentiCRISPR v.2 NDUFS1 gRNA1	http://genome-engineering.org/gecko/wp-content/uploads/2013/12/lentiCRISPRv2-and-lentiGuide-oligo-cloning-protocol.pdf	TAGAATGTATGCCTACTTGG	targeting gRNA sequence
sequence-based reagent	LentiCRISPR v.2 ALDOA gRNA1	http://genome-engineering.org/gecko/wp-content/uploads/2013/12/lentiCRISPRv2-and-lentiGuide-oligo-cloning-protocol.pdf	CATTGGCACCGAGAACACCG	targeting gRNA sequence
sequence-based reagent	LentiCRISPR v.2 SLC9A1 gRNA1	http://genome-engineering.org/gecko/wp-content/uploads/2013/12/lentiCRISPRv2-and-lentiGuide-oligo-cloning-protocol.pdf	GAGCAGGGTGCTGATGACGA	targeting gRNA sequence
sequence-based reagent	LentiCRISPR v.2 GJB2 gRNA1	http://genome-engineering.org/gecko/wp-content/uploads/2013/12/lentiCRISPRv2-and-lentiGuide-oligo-cloning-protocol.pdf	GACATAGAAGACGTACATGA	targeting gRNA sequence
Cell lines	Colorectal cancer cell lines	Bodmer laboratory, WIMM, Oxford		
Animal species	athymic Nude Crl:NU(NCr)-Foxn1nu	Charles River		

524

Cell lines and culture. Human colorectal cancer cell lines were provided by Professor Walter Bodmer and authenticated by gene sequencing (STR). Cell lines are regularly tested for mycoplasma contamination by antigen test. Cells were cultured using DMEM (Sigma-Aldrich, D7777) supplemented with 10% FBS and 1% PenStrep (10 000 U/mL) at 37°C and 5% CO_2. To adjust medium pH, the content of $NaHCO_3$ was varied (41).

siRNA transfection. Cells were seeded at a density of 200,000 cells/well in a 6 well plate and transfected with either siRNA (20nM), e.g. for *GJB2*, *GJB3* and *GJA1*, or with a scramble non-targeted siRNA (Dharmacon, siGENOME smart pool), using Lipofectamine RNAiMAX (Invitrogen, Cat. No. 2373383). After 72 hours, cells were harvested and seeded for experiments.

Viral transduction with CRISPR-CAS9 constructs. Gene knockouts were made for DLD1, SW1222 and HCT116 cell lines using DMEM, 10% FBS, 1% Pen/Strep. gRNA sequences were cloned into LentiCRISPR v.2 backbone as previously described (http://genome-engineering.org/gecko/wp-content/uploads/2013/12/lentiCRISPRv2-and-lentiGuide-oligo-cloning-protocol.pdf). Two gRNA sequences were cloned for each gene, using sequences below (Table 1). Concentrated virus aliquots were prepared by the virus production facility at WIMM, University of Oxford. Cells were plated in clear, flat-bottom 6-well plate at a density of 200,000 cells/well and transduced using a 500 µL aliquot of lentivirus carrying the LentiCRISPR v2 construct encoding for a gRNA sequence targeting one individual gene. Polybrene was added at a concentration of 4 µg/mL. The 6-well plate was incubated for 2 days before puromycin (5 µg/mL) was added for selection, and it was incubated for 3 days before the transduced cells were used for further experiments. Single cell clones with stable deletion of *NDUFS1* and *SLC9A1* were obtained in

SW1222 and HCT116 cells, respectively. Note that for *ALDOA* gRNA-treated DLD1 cells no stable knock-out clones could be obtained. Therefore, lentivirus pools of knockout cells were mixed populations of cells with different genomic edits and unedited cells. All growth curves were performed within one week of initial viral infection to avoid hypomorph or unedited cells out-competing those that have loss-of-function mutations.

NDUFS1 gRNA1	TAGAATGTATGCCTACTTGG
NDUFS1 gRNA2	TCACAAATAGGACAGTCCAA
ALDOA gRNA1	CATTGGCACCGAGAACACCG
ALDOA gRNA2	AATGGCGAGACTACCACCCA
SLC9A1 gRNA1	GAGCAGGGTGCTGATGACGA
SLC9A gRNA2	GATGCCAGACCGCAGAACCA
GJB2 gRNA1	GACATAGAAGACGTACATGA

Flow cytometric sorting. Cells were seeded on Petri dishes and harvested when confluent. Cells were resuspended in FACS-compatible solution containing 2% FBS in PBS and transferred to tubes for incubating with Ab for Cx43 APC-conjugated (R&D Systems cat.n. FAB7737A) for 45 min at RT. Cells were washed twice with FACS solution and sorted immediately thereafter. Positive and negative cells were collected, expanded, and prepared for western blotting for Cx43.

Spheroid growth. Wild-type and GJB2 KO (Cx26KO) DLD1 spheroids were prepared by the hanging drop method. 20 µl-drops with 400 DLD1 cells were allowed to form spheroids and grow for 72 hours. Spheroids were then collected and transferred into sterile non-TC flat bottom 96 plate (Falcon) pretreated with anti-

adherence rinsing solution (Stemcell Technologies, Cat.No. 07010) and imaged in brightfield setting using Cytation 5 plate reader to calculate radius.

Immunoblotting. Lysates were prepared with radioimmunoprecipitation assay (RIPA) buffer. Protein concentration in the samples was measured using bicinchoninic acid (BCA) protein assay kit and adjusted using water. Samples were loaded onto a 10% acrylamide gel. The gel was run at 120 V for 90 minutes. Afterwards, membrane transfer was performed at 250mA for 70 minutes. Membranes were incubated with primary antibodies against NDUFS1 (ThermoFisher Cat. No. PA5-22309), Aldolase A (Novus Biologicals, Cat. No. NBP1-87488), NHE1 (BD Biosciences, cat. No.611775), β-actin (Proteintech, Cat. No. HRP-60008) and GAPDH (Proteintech, Cat. No. HRP-60004) used as a loading control; Connexin26 (Thermo Fisher, Cat no. 13-8100), Connexin 31 (Proteintech, cat. No. 12880-1-AP), Connexin 43 (Thermo Fisher, Cat. No. Cat #13-8300), HRP-conjugated goat anti-rabbit and anti-mouse secondary antibodies were applied. The membrane was visualized using ECL.

Immunofluorescence. Cells were grown to 50–80% confluency, fixed with 4% paraformaldehyde in PBS (Pierce; Life Technologies) and permeabilized with 0.2% Triton X-100 in PBS. After blocking with 3% BSA in PBS for 1 h, cells were incubated with rabbit antibodies against Cx26 (Proteintech 14842-1-AP) and Cx43 (Cell signalling technology n.3512) for 1.5 hs at room temperature. Cells were then washed and incubated with Alexa Fluor 488 secondary antibody (Life Technologies) for 1 h. Cells nuclei were co-stained with Hoechst 33342 (Life Technologies) applied for 1 min following washing with 1X PBS. The mounting medium used was ProLong Gold Antifade reagent (Invitrogen, Cat. No. P36930).

Fluorescence Recovery After Photobleaching (FRAP) for measuring coupling. Monolayers in 4-well Ibidi imaging slides were loaded with calcein AM (Invitrogen, C1430) for 10 minutes in Hepes RPMI, replaced to remove unloaded dye. Confluent monolayers were imaged using Zeiss LSM 700 confocal microscope. A cell in the middle of a confluent cluster was selected for bleaching (high-power 488 nm) until fluorescence (488 nm excitation, emission >510 nm) decreased by 50%. Signal was measured in the central cell, neighbors and more remote cells, and normalized to the initial intensity. Recovery was fitted to a mono-exponential to calculate calcein permeability (units: μm/min) from product of the geometric perimeter and area of the central cell, divided by the time constant of fluorescence recovery. See Appendix 1 for details of calculation.

FRAP for measuring diffusivity. Cells were loaded with Violet (BMQC 5μM, excitation 405 nm, Invitrogen Cat.No. C10094), Green (CMFDA 20μM, excitation 492 nm, Cat.No. C2925), Orange (CMRA 20μM, 555 nm, Cat.No. C34551), or DeepRed (20μM, 630 nm, Cat.No. 34565) for 15 minutes in RPMI Hepes medium. FRAP was limited to a 3x3 μm region of cytoplasm.

Measuring the exchange of CellTracker dyes in terms of coupling coefficient. A suspension of cells was split equally, and each loaded with either CellTracker Violet or Orange for 15 min. Cells were pelleted, washed (PBS), combined in 1:1 ratio, and then seeded onto 4-well imaging slides at 300,000 cells/well. As control, cells were loaded with one type of dye. After 48 h, monolayers were imaged confocally using sequential acquisition that minimizes bleed-through between channels: 405 nm excitation and emission 490-555 nm for the Violet channel and 555 nm excitation and emission 560-600 nm for the Orange channel. Orange and violet fluorescence

615 were normalized to the mean signal in paired control. The degree of dye mixing was
616 quantified in terms of a coupling coefficient (CC):

$$\mathrm{CC} = 2 \times \min\left(\frac{\mathrm{F_O}}{(\mathrm{F_O} + \mathrm{F_V})}, \frac{\mathrm{F_V}}{(\mathrm{F_O} + \mathrm{F_V})}\right)$$

617 Here, F_O and F_V are the normalized Orange and Violet fluorescence signals. See
618 Appendix 1 for details of calculation.

619 **Measuring the exchange of CellTracker dyes by flow cytometry.** Cells were
620 loaded with combinations of CellTracker dyes, co-cultured for 48 h and processed for
621 flow cytometry (Attune NXT Analyser). Gain of detection channels was optimized by
622 analyzing monocultures loaded with one dye. Data were presented as pseudo-
623 colored bivariate density plots representing mono-cultures with the low-wavelength
624 dye as blue, mono-cultures with the high-wavelength dye as red, and co-cultures as
625 green.

626 **Measuring NHE1 activity**. Cells seeded on Ibidi 4-well slides were loaded with 10
627 μM cSNARF1 (Thermo Fisher, Cat. No. C1271, excitation, 555 nm; emission, 580
628 and 640 nm) for 7 minutes. Cells were then washed by superfusion with HEPES-
629 buffered normal Tyrode containing (in mM): NaCl (135), KCl (4.5), $CaCl_2$ (2), $MgCl_2$
630 (1), HEPES (20), glucose (11), pH adjusted to 7.4 with 4 M NaOH heated to 37°C.
631 After 2 min to allow equilibration, the superfusion was switched to ammonium
632 containing Tyrode (in mM): NaCl (105), NH_4Cl (30), KCl (4.5), $CaCl_2$ (2), $MgCl_2$ (1),
633 HEPES (20), glucose (11), pH adjusted to 7.4 with 4 M NaOH at 37°C. After 6 min,
634 the superfusate was returned to normal Tyrode. In some experiments, the solutions
635 contained 30 μM cariporide to block NHE1 (Tocris, Cat. No. 5358), as control. In
636 separate experiments, cSNARF1 fluorescence ratio was calibrated using the

637 nigericin method and this curve was used to convert measured cSNARF1 ratio to
638 pHi.

639 **Measuring resting pHi.** Cells were seeded at a density of 80,000 cells/well in Ibidi
640 flat bottom 96 well plates, to produce a monolayer after 24 h. On the measurement
641 day, cells were loaded dually with cSNARF1 (5 μg/ml) and Hoechst 33342 (1:1000)
642 for 15 min, followed by replacement with bicarbonate-free, Phenol Red-free medium
643 based on D5030, containing 10mM HEPES and MES and titrated at pH over the
644 range 6.2 to 7.7. Plates were imaged at Cytation 5 plate reader and each cell,
645 identified from the location of its nucleus, was analyzed for pHi (41). To measure
646 variation of pHi, the frequency distribution was offset to the mode pHi for each
647 experimental condition.

648 **Measuring medium acidification.** Cells were seeded at densities of 2,000 cells per
649 well on clear, flat-bottom 96-well plate (Ibidi). Cells were cultured in bicarbonate-
650 buffered media (D7777, Sigma) set to a pH of 7.4 by adjusting $NaHCO_3$ accordingly.
651 The cells were incubated for 4 days at 37°C with 5% CO_2 before media were
652 removed for glucose and lactate measurements.

653 **Pentra Assay for glucose and lactate.** Cells were seeded onto 96 well plates and
654 grown in DMEM (D7777, Sigma) at pH 7.4. After 5 days, medium was collected,
655 spun to remove residue, and analyzed in a Pentra C400 for glucose and lactate
656 concentrations. Calibrations used standard solutions.

657 **Measuring metabolic fluxes.** Two protocols were performed to measure metabolic
658 rate. The first interrogated glycolytic flux, and the second interrogated glycolysis and
659 respiration simultaneously. For the first, cells were cultured at high density (70,000
660 cells/well) in flat-bottom, black 96-well plates. To report extracellular pH, media
661 contained 50 μM cSNARF1-dextram. Media, based on DMEM D5030, contained

662 25mM glucose, 10% FBS, 1% PS, 1 mM pyruvate, 1% glutamax and 2 mM HEPES
663 and 2 mM MES to provide a low but constant buffering power over the pH range
664 studied. Fluorescence was monitored for 17 h using a Cytation 5 device (BioTek,
665 Agilent, Winooski, VT, USA). Excitation was provided by a monochromator, and
666 fluorescence emission was detected sequentially at wavelengths optimized as
667 described previously (42). For the second method, cells were cultured at high density
668 (70,000 cells/well) in flat-bottom, black 96-well plates. To report extracellular pH and
669 O_2, media contained 2 μM HPTS (8-Hydroxypyrene-1,3,6-trisulfonic acid trisodium
670 salt) and 50 μM RuBPY (tris(bipyridine)ruthenium(II) chloride). Media, based on
671 DMEM D5030, contained 25mM glucose, 10% FBS, 1% PS, 1 mM pyruvate, 1%
672 glutamax and 2 mM HEPES and 2 mM MES to provide a low but constant buffering
673 power over the pH range studied. Prior to measurements, each well was sealed with
674 150 μM mineral oil to restrict O_2 ingress. HPTS and RuBPY fluorescence were
675 monitored for 17 h using a Cytation 5 device (BioTek, Agilent, Winooski, VT, USA).
676 Excitation was provided by a monochromator, and fluorescence emission was
677 detected sequentially at five wavelengths, which were optimized as described
678 previously (42).

679 **Sulforhodamine B (SRB) and GFP growth assays.** GFP-labelled cells (pLV-eGFP
680 addgene plasmid # 36083) were transduced with lentiviral constructs. 48 h later cells
681 were seeded at 2,000 cells/well on flat-bottom 96-well plates (Ibidi). For co-cultures,
682 the ratio of the two cellular populations was varied. The following day, medium was
683 replaced with bicarbonate-buffered media (D7777, Sigma), and incubated at 37°C
684 with 5% CO_2 for seven days; in some experiments, atmospheric O_2 was reduced to
685 2% to produce hypoxia. For some experiments, incubations were terminated on days
686 2, 3, 4, 5, 6 and 7 to obtain a time course. Plates were analyzed for GFP

fluorescence and SRB absorbance (Cytation 5). The GFP signal was measured in intact monolayers (excitation 490 nm, emission 520 nm). Next, wells were prepared for the SRB assay by fixing with PFA 4% for 30 min, washing with water and staining with 100 μL 0.057% SRB (in 1% acetic acid) for 30 min. Residual SRB was removed by washing with 1% acetic acid four times. Finally, 200 μL/well 10 mM Tris base was added to release SRB and measure absorbance (520 nm).

***In vivo* xenograft experiments.** 6-week old female athymic Nude Crl:NU(NCr)-Foxn1nu mice were injected sub-cutaneously with a 1:1 mixture of either wild-type DLD1 cells and GFP-labelled *NDUFS1* KO SW1222 cells or a 1:1 mixture of *GJB2* KO DLD1 cells and GFP-labelled *NDUFS1* KO SW1222 cells. CRCs cells were resuspended in 100 μL of a 1:1 mixture of Matrigel and serum-free DMEM medium before injection. Each mouse was injected with 2 million cells to each flank: WT DLD1+*NDUFS1* KO SW1222 on left and *GJB2* KO DLD1 cells+*NDUFS1* KO SW1222 on right. Mice were weighed and tumors were measured 3 times a week. At the end of the experiments, when tumors reached the scientific or humane endpoint, mice were sacrificed and tumors excised and processed for imaging. Tumour cryo-sections were cut (ThermoFisher Scientific cryostat) across the tumor height to slices of thickness 5 microns. Sections were then stained with Hoechst and anti-GFP polyclonal antibody (ThermoFisher #A-11122) to enhance the signal from GFP-expressing *NDUFS1*-deficient SW1222 cells. Briefly: frozen slides were air-dried for 30 min, relevant sections marked with a pap-pen ring, and then slides were dip-washed in PBS for 10 min (staining jar), dried with tissue and placed in staining chamber tray, blocked with PBS Triton 0.1% with 5% goat serum and 2% BSA for 30 min, rinsed with PBS 3x (using 3 ml pipette), incubated with primary anti-GFP antibody in PBS Triton 0.1% at 1:250 dilution and 2% goat serum for 1 hour, rinsed

712 3x with PBS, incubated with secondary antibody (goat anti rabbit Alexa 488) at
713 1:1000 and Hoechst-33258 in PBS Triton 0.1% for 30min, rinsed 1x with PBS and
714 then dip-washed in PBS for 2min, then dried with tissue. ~35 µl of slow-fade
715 diamond (Thermo Fisher, S36963) was added and a coverslip applied and sealed
716 with nail polish. Every 5th slides was imagined using a Zeiss Axioscan slide scanner
717 using a 20x0.8 Plan-Apochromat objective. The montage of images was constructed
718 for the Hoechst and GFP channels. To demarcate the area of the tumour, the
719 Hoechst signal was dilated (rolling ball, 50 pixels) to expand beyond nuclei and fused
720 to form a mask, with smaller particles ignored. The background of GFP images was
721 calculated from the mean of fluorescence within the Hoechst-defined tumour mask.
722 To produce a thresholded GFP image, pixels were defined as GFP-positive if their
723 fluorescence exceeded 4, 5, or 6 standard deviations from the mean GFP signal
724 within the masked region; all other pixels were re-assigned a GFP value of zero.
725 Next, all GFP-positive clusters were counted (ignoring large particles which are likely
726 non-cellular stains) and the total area calculated. Each slide also provided a
727 measure of tumour area. The total GFP-positive cluster count and area, and overall
728 tumour area were summed over all slices. The analyses were repeated for the three
729 levels of thresholding to ensure the findings are consistent.

730 **Statistics**. Data expressed as mean±SEM. Significance: *=P<0.05, **=P<0.01,
731 ***=P<0.001. Gaussian mixture modelling was performed using GMMchi
732 (https://github.com/jeffliu6068/GMMchi). Before selecting tests, data were tested for
733 normality by the Kolmogorov-Smirnov test. One-sample t-tests were performed to
734 compare data against an expected value (for data failing normality test, the non-
735 parametric test was the Wilcoxon signed rank test). For comparisons between two or
736 more samples, one-way ANOVA was performed.

ACKNOWLEDGEMENTS: The work was supported by the European Research Council, SURVIVE #723997. We thank Professor Alison Simmons and Dr Agne Antanaviciute for access to the single-cell RNA GSE datasets for colonic epithelium.

COMPETING INTERESTS: None to declare.

DATA AVAILABILITY STATEMENT: All data generated or analysed during this study are included in this published article and its supplementary information files.

REFERENCES

1. Nowell PC. The clonal evolution of tumor cell populations. Science **1976**;194:23-8
2. Merlo LM, Pepper JW, Reid BJ, Maley CC. Cancer as an evolutionary and ecological process. Nat Rev Cancer **2006**;6:924-35
3. Wolfl B, te Rietmole H, Salvioli M, Kaznatcheev A, Thuijsman F, Brown JS*, et al.* The Contribution of Evolutionary Game Theory to Understanding and Treating Cancer. Dyn Games Appl **2021**
4. Johnston MD, Edwards CM, Bodmer WF, Maini PK, Chapman SJ. Mathematical modeling of cell population dynamics in the colonic crypt and in colorectal cancer. Proc Natl Acad Sci U S A **2007**;104:4008-13
5. Tomlinson IP, Bodmer WF. Failure of programmed cell death and differentiation as causes of tumors: some simple mathematical models. Proc Natl Acad Sci U S A **1995**;92:11130-4
6. Gillies RJ, Verduzco D, Gatenby RA. Evolutionary dynamics of carcinogenesis and why targeted therapy does not work. Nat Rev Cancer **2012**;12:487-93
7. Greenman C, Wooster R, Futreal PA, Stratton MR, Easton DF. Statistical analysis of pathogenicity of somatic mutations in cancer. Genetics **2006**;173:2187-98
8. Wang T, Birsoy K, Hughes NW, Krupczak KM, Post Y, Wei JJ*, et al.* Identification and characterization of essential genes in the human genome. Science **2015**;350:1096-101
9. Blomen VA, Majek P, Jae LT, Bigenzahn JW, Nieuwenhuis J, Staring J*, et al.* Gene essentiality and synthetic lethality in haploid human cells. Science **2015**;350:1092-6
10. Sinkala M, Mulder N, Patrick Martin D. Metabolic gene alterations impact the clinical aggressiveness and drug responses of 32 human cancers. Commun Biol **2019**;2:414
11. Denko NC. Hypoxia, HIF1 and glucose metabolism in the solid tumour. Nat Rev Cancer **2008**;8:705-13
12. Zapata L, Pich O, Serrano L, Kondrashov FA, Ossowski S, Schaefer MH. Negative selection in tumor genome evolution acts on essential cellular functions and the immunopeptidome. Genome Biol **2018**;19:67
13. Bailey MH, Tokheim C, Porta-Pardo E, Sengupta S, Bertrand D, Weerasinghe A*, et al.* Comprehensive Characterization of Cancer Driver Genes and Mutations. Cell **2018**;174:1034-5
14. Martincorena I, Raine KM, Gerstung M, Dawson KJ, Haase K, Van Loo P*, et al.* Universal Patterns of Selection in Cancer and Somatic Tissues. Cell **2017**;171:1029-41 e21

15. Dovmark TH, Hulikova A, Niederer SA, Vaughan-Jones RD, Swietach P. Normoxic cells remotely regulate the acid-base balance of cells at the hypoxic core of connexin-coupled tumor growths. FASEB J **2018**;32:83-96
16. Dovmark TH, Saccomano M, Hulikova A, Alves F, Swietach P. Connexin-43 channels are a pathway for discharging lactate from glycolytic pancreatic ductal adenocarcinoma cells. Oncogene **2017**;36:4538-50
17. Aasen T, Mesnil M, Naus CC, Lampe PD, Laird DW. Gap junctions and cancer: communicating for 50 years. Nat Rev Cancer **2016**;16:775-88
18. Nicholson BJ. Gap junctions - from cell to molecule. J Cell Sci **2003**;116:4479-81
19. Gilula NB, Reeves OR, Steinbach A. Metabolic coupling, ionic coupling and cell contacts. Nature **1972**;235:262-5
20. Pitts JD. The discovery of metabolic co-operation. Bioessays **1998**;20:1047-51
21. Fujimoto WY, Subak-Sharpe JH, Seegmiller JE. Hypoxanthine-guanine phosphoribosyltransferase deficiency: chemical agents selective for mutant or normal cultured fibroblasts in mixed and heterozygote cultures. Proc Natl Acad Sci U S A **1971**;68:1516-9
22. Loewenstein WR, Kanno Y. Intercellular communication and the control of tissue growth: lack of communication between cancer cells. Nature **1966**;209:1248-9
23. Spray DC, Hanstein R, Lopez-Quintero SV, Stout RF, Jr., Suadicani SO, Thi MM. Gap junctions and Bystander Effects: Good Samaritans and executioners. Wiley Interdiscip Rev Membr Transp Signal **2013**;2:1-15
24. Mesnil M, Piccoli C, Tiraby G, Willecke K, Yamasaki H. Bystander killing of cancer cells by herpes simplex virus thymidine kinase gene is mediated by connexins. Proc Natl Acad Sci U S A **1996**;93:1831-5
25. Pitts JD. Cancer gene therapy: a bystander effect using the gap junctional pathway. Mol Carcinog **1994**;11:127-30
26. Bi WL, Parysek LM, Warnick R, Stambrook PJ. In vitro evidence that metabolic cooperation is responsible for the bystander effect observed with HSV tk retroviral gene therapy. Hum Gene Ther **1993**;4:725-31
27. Counillon L, Bouret Y, Marchiq I, Pouyssegur J. Na(+)/H(+) antiporter (NHE1) and lactate/H(+) symporters (MCTs) in pH homeostasis and cancer metabolism. Biochim Biophys Acta **2016**;1863:2465-80
28. Ritterson Lew C, Tolan DR. Targeting of several glycolytic enzymes using RNA interference reveals aldolase affects cancer cell proliferation through a non-glycolytic mechanism. J Biol Chem **2012**;287:42554-63
29. Urra FA, Munoz F, Lovy A, Cardenas C. The Mitochondrial Complex(I)ty of Cancer. Front Oncol **2017**;7:118

30. Wilding JL, McGowan S, Liu Y, Bodmer WF. Replication error deficient and proficient colorectal cancer gene expression differences caused by 3'UTR polyT sequence deletions. Proc Natl Acad Sci U S A **2010**;107:21058-63
31. Fawkner-Corbett D, Antanaviciute A, Parikh K, Jagielowicz M, Geros AS, Gupta T*, et al.* Spatiotemporal analysis of human intestinal development at single-cell resolution. Cell **2021**;184:810-26 e23
32. Sirnes S, Lind GE, Bruun J, Fykerud TA, Mesnil M, Lothe RA*, et al.* Connexins in colorectal cancer pathogenesis. Int J Cancer **2015**;137:1-11
33. Dubina MV, Iatckii NA, Popov DE, Vasil'ev SV, Krutovskikh VA. Connexin 43, but not connexin 32, is mutated at advanced stages of human sporadic colon cancer. Oncogene **2002**;21:4992-6
34. Swietach P, Monterisi S. A Barter Economy in Tumors: Exchanging Metabolites through Gap Junctions. Cancers (Basel) **2019**;11
35. Hulikova A, Harris AL, Vaughan-Jones RD, Swietach P. Regulation of intracellular pH in cancer cell lines under normoxia and hypoxia. J Cell Physiol **2013**;228:743-52
36. Michl J, Wang Y, Monterisi S, Blaszczak W, Beveridge R, Bridges EM*, et al.* CRISPR/Cas9 screen identifies oxidative phosphorylation as essential for cancer cell survival at low extracellular pH. Cell Rep **2022**;In press
37. Koval M, Molina SA, Burt JM. Mix and match: investigating heteromeric and heterotypic gap junction channels in model systems and native tissues. FEBS Lett **2014**;588:1193-204
38. Kanczuga-Koda L, Sulkowski S, Koda M, Sulkowska M. Alterations in connexin26 expression during colorectal carcinogenesis. Oncology **2005**;68:217-22
39. Tomlinson IP, Bodmer WF. Modelling the consequences of interactions between tumour cells. Br J Cancer **1997**;75:157-60
40. Bertolaso M, Dieli AM. Cancer and intercellular cooperation. R Soc Open Sci **2017**;4:170470
41. Michl J, Park KC, Swietach P. Evidence-based guidelines for controlling pH in mammalian live-cell culture systems. Commun Biol **2019**;2:144
42. Blaszczak W, Tan Z, Swietach P. Cost-Effective Real-Time Metabolic Profiling of Cancer Cell Lines for Plate-Based Assays. Chemosensors **2021**;9

FIGURE LEGENDS

Figure 1: *Connexin isoform expression in CRC cells.* (A.) Microarray data from 79 CRC cell lines analyzed for message level of seven connexin genes. Frequency distributions for $\log_2$-transformed data. A Gaussian mixture modelling based analysis (GMMchi) is used to determine whether the distributions are bimodal or unimodal. Vertical red line is the (cut-off threshold separating low/high groups. Pink bars refer to background levels and yellow bars refer to near-background levels, based on a separate analysis of the overall pattern of gene expression observed in the cell lines. The cut-off thresholds for the difference between low and high expression are: $2^{6.2}$, $2^{4.9}$, $2^{7.5}$, $2^{6.3}$, and $2^{7.1}$ for *GJA1*, *GJA3*, *GJB1*, *GJB5*, and *GJC1*, respectively. (B.) Analysis of single-cell RNAseq datasets for normal colon obtained from the GSE116222 dataset available at the Gene Expression Omnibus (https://www.ncbi.nlm.nih.gov/geo/query/acc.cgi?acc=GSE116222). Bars show mean expression levels by cell type. (C.) Two-by-two table shows correlation between bimodally distributed connexin genes. Numbers refer to correlation coefficient for significant ($p<0.05$) gene pairs (Fisher's exact test). (D.) Log_2-transformed expression data ranked by the sum of *GJB2* and *GJB3* expression. Cells selected for further studies are indicated by a dot above the heatmap. (E.) Heatmap replotted for the selected 15 cell lines, grouped by *GJA1* and *GJC1* expression, relative to threshold determined from GMM analysis. (F.) Western blot for Cx43, showing agreement between protein levels and gene expression profiles.

Figure 2: *Connexin isoforms underpinning cell-to-cell coupling in CRC cells.* (A.) FRAP protocol for interrogating the apparent ,cell-to-cell permeability to calcein in RKO cells (connexin-null) and SNU1235 cells (Cx26-positive). Images taken before bleaching (resting), immediately after bleach, and 5 min after bleach. (B.) Apparent permeability to calcein (mean±SEM) in CRC monolayers; * denotes significant coupling (t-test). For each experiment, measurements were obtained from at least 5 independently grown monolayers, with multiple technical repeats each. N=15-80 per line. (C.) FRAP measurements repeated in the presence of 100 μM carbenoxolone (CBX). (D/E.) FRAP measurements on cells transfected with siRNA to knockdown *GJA1*, *GJB3* or *GJB2*. Data normally distributed (Kolmogorov-Smirnov test). Statistical test by one-way ANOVA. * denotes significant decrease in permeability relative to scrambled construct control. (F.) Immunofluorescence in monolayers showing nuclei stained with DAPI (blue) and connexin Cx26 (green), where present. (G.) Immunofluorescence performed with Cx43 antibody (green). Images ranked by increasing connexin signal at cell-to-cell contacts. (H.) Western blot of LOVO and Caco2 sub-populations following FAC-sorting by Cx43-status. (I.) Confirmation that sgRNA or siRNA against *GJB2* decreases the expression of Cx26 in DLD1 and SW1222 cells. (J.) siRNA knockdown of *GJB2* eliminates Cx26 immunofluorescence signal at cell-to-cell contacts in SW1222 cells. (K.) Blot for Cx26 in DLD1 cells and knockout (KO1-3) clones, and confocal image of Calcein-loaded monolayers established from for WT or KO1 cells. (L.). Confluent DLD1 *GJB2* KO (clone 1) monolayers had substantially reduced cell-cell connectivity, as determined by FRAP. Mean±SEM of 20 cells from 3 monolayers for each genotype. Data normally distributed (Kolmogorov-Smirnov test). Statistical test by one-way ANOVA. *** denotes significant difference ($P<0.001$) from WT.

Figure 3: *Fluorescent molecules equilibrate between coupled cells: imaging.* (A.) Representative time courses of FRAP protocol for measuring cytoplasmic diffusivity of CellTracker dyes in DLD1 cells in sparse culture. (B.) Mean recovery rate constant as a function of the molecular weight of the CellTracker dye. Mean±SEM; N=20-25 DLD1 cells (star symbol), 7-15 LOVO cells (circles). (C.) Schematic for preparing co-cultures or monocultures loaded with CellTracker dyes. (D.) Confocal imaging of DLD1 monolayers. CellTracker orange is pseudocolored red and CellTracker Violet is pseudocolored blue; mixing produces purple appearance. (E.) Images of co-cultures from eight CRC lines, ranked by increasing *GJB2* message, acquired from confluent and low-confluency regions. (F.) Exemplar images of monolayers established from high and low density cultures, showing more exchange where cells make extensive cell-to-cell contacts. For comparison, RKO cells shown at high density; these cells do not express connexin genes. (G.) Quantification of dye exchange in terms of coupling coefficient. Note that mono-cultures produce no (Violet) or very low (Orange) coupling coefficients (see Supplement).. Mean±SEM of multiple fields of view from 4-7 biological repeats. Shaded data indicate data from "low" seeding density i.e. low coupling. # denotes significant ($P<0.05$) difference between low and high seeding density, performed pairwise for OXCO1 and DLD1 cells. (H.) Frequency distribution of coupling coefficient ranked by decreasing coupling strength.

Figure 4: *Fluorescent molecules equilibrate between coupled cells: cytometry.* (A.) Schematic for producing monocultures or co-cultures with pairs of CellTracker dyes. (B.) Cytometry of DLD1 monocultures grown from cells loaded with either DeepRed or Orange, or co-cultures grown from 1:1 mix of cells loaded with DeepRed and

923 Orange. Logarithmic axes showing signal on the relevant detection channels.
924 CellTracker Orange monocultures emit signal on the orange detection channel only;
925 CellTracker DeepRed monocultures emit signal on the DeepRed detection channel
926 only; co-cultures emit fluorescence on both detection channels (indicating that dye
927 exchange had taken place). Overlay shows pseudo-colored bivariate density maps:
928 red for Orange mono-cultures, blue for Deep-Red mono-cultures and green for co-
929 cultures. Arrow points to cluster showing evidence for dye exchange. (C.) Flow
930 Cytometry of DLD1 cells that were grown as monocultures labeled with either
931 DeepRed or Orange. Aliquots of DeepRed- and Orange-labelled cells were mixed
932 prior to flow cytometry to test for acute dye exchange. Analyses show no evidence
933 for dye exchange between acutely mixed cell suspensions. (D.) Cytometry of co-
934 cultured or acutely mixed DLD1, (E.) HT29, (F.) OXCO1 or (G) C10 cells loaded with
935 various pairs of CellTracker dyes. (H.) Quantification of the fraction of cells that had
936 exchanged CellTracker dyes. Region thresholds defined by 95th percentile of signal
937 detected on channels. Significant dye exchange took place only in co-cultured cells
938 but not acutely mixed cells. Significance testing by t-test: **** is P<0.0001. Each
939 data point represents a separate batch of cells processed for flow cytometry.

940

941 **Figure 5:** *Diffusive coupling rescues genetically-inactivated Na^+/H^+ exchange*
942 *function.* (A.) Western blot for NHE1, product of *SLC9A1* in wild-type HCT116 and
943 two KO clones. gRNA for KO1 produced a truncated protein, whereas gRNA for
944 KO2 produced complete ablation of expression. (B.) Functional confirmation of
945 genetic inactivation of *SLC9A1*. Measurements of intracellular pH (pHi) in HCT116
946 monolayers: following acid-loading by ammonium prepulse (absence of CO_2/HCO_3^-
947 buffer), NHE1 activity in wild-type (WT) cells mediates recovery of pHi (N=13

biological repeats, with 3 technical repeats each), blocked pharmacologically with cariporide (30 μM; N=6 biological repeats, with 3 technical repeats each). KO clones (N=7-9 biological repeats, with 3 technical repeats each) produce no NHE1 activity. Mean±SEM. (C.) Co-culture of WT and KO HCT116 cells. Cells loaded with cSNARF to stain cytoplasm; GFP fluorescence emitted from KO cells. (D.) Ammonium prepulse performed on co-cultures, separating signal from WT (GFP-negative: black) and KO cells (GFP-positive: green). Mean±SEM (N=9-13 biological repeats, with 3 technical repeats each). For comparison, dotted line shows results from WT or KO monocultures. (E.) Relationship between extracellular and intracellular pH measured in HEPES-MES buffered media (absence of CO_2/HCO_3^- buffer) for WT cells, *GJB2* knockdown cells, or *SLC9A1* KO cells. Results from clone 1 and clone 2 were not significantly different and pooled together. Measurements were performed for monocultures or co-cultures. Mean±SEM (clockwise: N=6 WT and 6 WT *sgGJB2* monocultures; 6 WT and 7 KO monocultures; 8 WT+KO co-cultures; 6 WT sg*GJB2*+KO co-cultures; each with 6 technical repeats). Statistical testing by two-way ANOVA for pH and genotype; effect of genotype reported in figure (*** denotes P<0.001). (F.) Analysis of pHi data from E in terms of frequency distribution of pHi, offset to the mode. (G.) Growth curves for HCT116 cells grown as co-cultures of various ratios of WT and KO2 cells, quantified in terms of GFP fluorescence (KO compartment) and SRB absorbance (total biomass) over 7 days of culture, starting from a seeding density of 2,000 cells/well. Mean±SEM (N=5 per construct, with 4 technical repeats each). Significant enrichment indicates that the KO compartment expanded faster than expected from the SRB curve and seeding ratio (2,000:0, 1500:500, 1000:1000, 500:1500 and 0:2000), indicating that KO cells benefited from coupling onto WT neighbors. Statistical testing by two-way ANOVA

between GFP time course and SRB time course scaled by initial seeding ratio (e.g. 0.5 for 1:1 co-culture); P value reported for difference between measured growth of KO2 cells (GFP) and prediction growth (SRB, scaled by KO2:WT seeding ratio). Significance at $P<0.05$ indicated by shading between measured (green) and predicted (cyan) time course. Media were at pH 7.4. Bar graph shows GFP signal at Day 7 of culture. Grey line is predicted signal. Significant enrichment of GFP cells for seeding ratios of 1:1 and 1:3 (KO2:WT). (H.) Experiments repeated using media at pH 6.6.

Figure 6: *Diffusive coupling rescues genetically-inactivated glycolysis.* (A.) Western blot for aldolase A (ALDOA) in wild-type (WT) DLD1 cells and cells infected with one of two guide RNA constructs to genetically inactivate *ALDOA*. (B.) Medium acidification measured in confluent DLD1 cells in low-buffer power media (2mM HEPES+MES). WT cells are highly glycolytic, as measured from the acidification time course. Glycolytic rate is greatly reduced by *ALDOA* ablation. Mean±SEM (N=4 plates, each with 3 technical repeats). (C.) DLD1 cells cultured for 4 days in CO_2/HCO_3^- buffered media. Media collected at end-point were assayed for glucose and lactate. Mean±SEM (N=3 plates, each 3 technical repeats pooled per assay). ** denotes significant difference ($P<0.01$) in glucose consumption relative to WT; ## denotes significant difference ($P<0.01$) in lactate production relative to WT; testing by one-way ANOVA and multiple comparisons test. Normality test by Kolmogorov-Smirnov test. (D.) Co-culture of WT and *ALDOA*-deficient DLD1 cells. Cells loaded with cSNARF-1 to indicate cytoplasm; GFP fluorescence emitted from gRNA-infected cells. (E). GFP fluorescence and SRB absorbance after 6 days of culture of various seeding ratios of WT and *ALDOA*-deficient cells infected with construct #1:

2000:0, 1500:500, 1000:1000, 500:1500 and 0:2000. Left: grey line shows expected GFP signals if growth of WT and *ALDOA*-deficient cells were no different. Right: gray line shows expected SRB signal if growth of WT and *ALDOA*-deficient cells were no different. Significance testing by t-test relative to gray line. Mean±SEM (N=5 plates, 6 technical repeats each). Normality test by Kolmogorov-Smirnov test. Significance testing by one-sample t-test relative to expected value (shown as grey line). (F.) Experiment repeated with construct 2. Mean±SEM (N=5 plates, 6 technical repeats each). (G.) Experiment repeated after *GJB2* gRNA treatment to knockout *GJB2* in WT cells, i.e. inactivating connexin coupling between WT and *NDUFS1*-deficient cells. Mean±SEM (N=3 plates, 6 technical repeats each). (H.) Co-culture experiment of wild-type C10 cells with GFP-labelled ALDOA-deficient C10 cells (gRNA #1). Mean±SEM (N=5 plates, 6 technical repeats each). (I.) Co-culture experiment of wild-type NCIH747 cells with GFP-labelled ALDOA-deficient NCIH747 cells (gRNA #1). Mean±SEM (N=4 plates, 6 technical repeats each).

Figure 7: *Diffusive coupling rescues genetically-inactivated mitochondrial respiration.* (A.) Western blot for NDUFS1 in wild-type (WT) SW1222 cells and *NDUFS1* KO clones established using one of two guide RNAs. (B.) Fluorimetric measurements of oxygen consumption and acid production (assays of respiratory and glycolytic rates) in WT and *NDUFS1* KO SW1222 cells. Mean±SEM (N=3 plates, 3 technical repeats each). (C.) Co-culture of WT and *NDUFS1* KO cells. Cells loaded with cSNARF-1 to indicate cytoplasm; GFP fluorescence emitted from KO cells. (D) GFP fluorescence and SRB absorbance after 6 days of culture of various seeding ratios of WT and *NDUFS1*-deficient cells infected with construct #1: 2000:0, 1500:500, 1000:1000, 500:1500 and 0:2000. Left: grey line shows expected GFP

signals if growth of WT and *NDUFS1*-deficient cells were no different. Right: gray line shows expected SRB signal if growth of WT and *NDUFS1*-deficient cells were no different. Media pH set to 7.7. Significance testing by t-test relative to gray line. Mean±SEM (N=4 plates, 4 technical repeats each). Normality test by Kolmogorov-Smirnov test. Significance testing by one-sample t-test relative to expected value (shown as grey line). (E.) Experiment repeated at lower (1000/well) seeding density to reduce incidence of cell coupling. Mean±SEM (N=4 plates, 6 technical repeats each). (F.) Experiment repeated with WT cells *GJB2* KD via siRNA, i.e. inactivating connexin coupling between WT and *NDUFS1*-deficient cells. Mean±SEM (N=3 plates, 6 technical repeats each). (G.) Experiment repeated under hypoxic conditions, which suppresses mitochondrial function. Mean±SEM (N=4 plates, 6 technical repeats). (H.) Co-culture of GFP-labelled *NDUFS1* KO cells (#1) with one of three Cx26-negative cells: wild-type RKO, C10 or NCIH747 cells.

Figure 8: *Metabolic rescue by connexins channels.* (A.) Western blot for Cx26, showing absence of protein in *GJB2* KO DLD1 cells. RKO used as negative control. (B.) Effect of Cx26 (*GJB2*) knockdown on DLD1 cell growth in 2-D monolayer (n=4; not significant, paired t-test). Seeded at 2,000 per well, growth after 6 days measured by SRB assay (absorbance, 520 nm). (C.) Effect of Cx26 (*GJB2*) knockdown on ability of DLD1 cell to form spheroids (n=3 platings, each yielding 60-80 spheroids; not significant, nested paired t-test). (D.) Growth curves of xenografts on left and right flank of nude female mice (n=6). Analysis by repeated measures two-way ANOVA (* $P<0.05$, ***$P<0.001$). Time courses aligned to end-point. (E.) Histology of selected 5-μm slices through the middle of a xenograft on the left or right flank (matched animal). Panels show (i) staining for Hoechst, (ii) GFP signal from

antibody, (iii) GFP signal in a central area of the field of view, after removing background (thresholding), (iv) analysis of GFP-positive clusters (indicated by green dot) within outline (red) of tumor mass. Scale bar is 1 mm. (F.) Results of analysis of left and right flank xenografts from six mice in terms of tumor area, number of GFP-positive clusters, and ensemble area of GFP-positive clusters. (G.) Cartoon summary of the role of connexin channels, particularly Cx26 (green conduits) in rescuing cell carrying mutations in an enzyme (E^{mut}) and membrane transporter (T^{mut}). Itself, the mutation-bearing cell is unable to convert substrate A to B (by enzyme E) and take-up substance C. However, these functions can be rescued by diffusive exchange of A, B and C with neighboring cells that express wildtype T^{wt} and E^{wt}. (H.) Scenario i: A wild-type cell survives and divides. Scenario ii: In isolation or in mono-culture, a mutation-bearing cell cannot survive and fails to divide and therefore carry on its genetic mutation. In a human tumor, this would lead to negative selection of such loss-of-function mutations in important genes (coding for E and T). Scenario iii: Coupling onto wild-type cells can rescue the metabolic defect of the mutation-bearing cell, hence allowing survival. These mutations will carry on to daughter cells and therefore not lead to negative selection.

SUPPLEMENTARY FILES AND FIGURE LEGENDS

Supplementary File 1: Correlation between connexin expression and functional coupling.

Figure 1-figure supplement 1: Application of GMMchi pipeline in purifying non-tumor expression from bulk tumor expression in the TCGA patient samples revealed that out of 689 TCGA CRC samples, 51 are paired normal samples and 637 tumor samples. Graphs show the expression distribution of the *GJA1*, *GJA3*, *GJB1*, *GJB2*, *GJB3*, *GJB5*, and *GJC1* combining paired tumor and normal samples.

Figure 1-figure supplement 2: Principal component analysis (PCA) of microarray data covering all studied CRC lines, showing weights for the seven Cx genes (i.e. a 77 by 7 matrix of gene expression data). Analysis by MATLAB's pca function. The analysis describes the connexin expression pattern for each cell line, and plots this on two axes (PC1 and PC2), which explain 52% and 16% of variability, respectively. Note the correlation between *GJB2* and *GJB3*.

Figure 2-figure supplement 1: Western blot analysis of the effects of connexin 26, 31 or 43 gene knockdown on the expression of selected connexin isoforms in DLD1 and C10 cells, including confirmation of knockdown efficacy.

Figure 2-figure supplement 2: Confirmation of the knockdown efficiency of siRNA construct against *GJA1* (Cx43) in C10 cells. Actin used as loading control.

Figure 3-figure supplement 1: Confirmation that monocultures of one CellTracker dye only produce negligible coupling coefficients, as expected from the absence of a second dye.

Figure 5-figure supplement 1: Growth curves for HCT116 cells grown as co-cultures of various ratios of WT and KO1 cells, quantified in terms of GFP fluorescence (KO compartment) and SRB absorbance (total biomass) over 7 days of culture, starting from a seeding density of 2,000 cells/well. Mean±SEM (N=5 per construct, with 3 technical repeats each). Significant enrichment indicates that the KO compartment expanded faster than expected from the SRB curve and seeding ratio (2000:0, 1500:500, 1000:1000, 500:1500 and 0:2000), indicating that KO cells benefited from coupling onto WT neighbors. Statistical testing by two-way ANOVA; P value reported for difference between measured growth of KO cells (GFP) and prediction growth (SRB, scaled by KO:WT seeding ratio). Yellow shading denotes significance at $P<0.05$. Media were at pH 7.4 or 6.6.

Figure 6-figure supplement 1: SRB absorbance after 6 days of culture of *ALDOA*-deficient cells infected with construct #1 or #2, normalized to time-matched WT cells. One-way ANOVA, pairwise testing.

Figure 6-figure supplement 2: GFP fluorescence after 6 days of culture of various seeding ratios of WT RKO cells with *ALDOA*-deficient DLD1 cells: 2000:0, 1500:500, 1000:1000, 500:1500 and 0:2000. Grey line shows expected GFP signals if growth of *ALDOA*-deficient cells was not supported by coupling onto WT cells. Media pH set to 7.4. Significance testing by t-test relative to gray line. Mean±SEM (N=4 plates, 4 technical repeats each). Normality test by Kolmogorov-Smirnov test. Significance testing by one-sample t-test relative to expected value (shown as grey line).

Figure 6-figure supplement 3: Western blot confirmation of the effect of siRNA knockdown of *ALDOA* on protein levels.

Figure 7-figure supplement 1: SRB absorbance after 6 days of culture of *NDUFS1*-deficient cells, normalized to time-matched WT cells. T-test.

Figure 8-figure supplement 1: Analysis of xenograft histology using three levels of threshold to define GFP-positive areas. The overall conclusions are not affected by the choice of threshold. Threshold of 5 standard deviation above mean background was selected for analysis in Figure 8. ID on x axis denotes mouse; blue are data from left flank, red are data from right flank.

Full length gels

Figure 1-source data 1: full length scans of blots for Figure 1F.

Figure 2-figure supplement 1-source data 1: full length scans of blots for Figure 2-supplement 1 panels A-F.

Figure 2-figure supplement 2-source data 1:: full length scans of blots for Figure 2-supplement 2.

Figure 2-source data 1: full length scans of blots for Figure 2H, 2I and 2K.

Figure 5-source data 1: full length scans of blots for Figure 5A.

Figure 6-figure supplement 3-source data 1: full length scans of blots for panels A and B.

Figure 6-source data 1: full length scans of blots for Figure 6A.

Figure 7-source data 1: full length scans of blots for Figure 7A.

Figure 8-source data 1: full length scans of blots for Figure 8A.

APPENDIX 1

1. CALCULATING PERMEABILITY FROM FRAP RECORDINGS:

Permeability to calcein across cell-to-cell junctions was measured in monolayers where cells made contacts between one another. A cell within a confluent structure was selected for bleaching. Permeability to calcein, in units of μm/s, was measured from the FRAP recovery time course measured in the bleached cell, and geometrical information obtained from the image of the monolayer.

The principle behind calculating permeability P is equation 1:

$$dC_{cell}/dt = \rho \cdot P \cdot (C_{cell} - C_{surround}) \quad [1]$$

Where subscripts 'cell' and 'surround' refer to the central cell and its cellular neighbours, respectively, and ρ is the ratio of the surface area of the barrier (i.e. membrane) and the cell volume.

In the experiment, fluorescence (F) is a readout of concentration (C), normalized by a scalar α:

$$C = \alpha \cdot F$$

Thus, the rate of recovery (LHS of equation [1]) is:

$$dC/dt = d(\alpha \cdot F)/dt = \alpha \cdot dF/dt \quad [2]$$

And the RHS of equation [1] becomes:

$$P \cdot (C_{cell} - C_{surround}) = P \cdot (\alpha \cdot F_{cell} - \alpha \cdot F_{surround}) = \alpha \cdot P \cdot (F_{cell} - F_{surround}) \quad [3]$$

Putting [2] and [3] together cancels out α:

$$dF_{cell}/dt = \rho \cdot P \cdot (F_{cell} - F_{surround})$$

Prior to bleaching, there are no net gradients, thus initial F_{cell} and $F_{surround}$ are equal. To account for this, fluorescence F in the cell and its surroundings can be normalized to starting signals:

$$f = F/F_0$$

Thus, equation [1] becomes:

$$df_{cell}/dt = \rho \cdot P \cdot (f_{cell} - f_{surround})$$

P can therefore be expressed as:

$$P = df_{cell}/dt \; / \; (\rho \cdot (f_{cell} - f_{surround}))$$

Here, df_{cell}/dt is measured from the fluorescence recovery time course. This is the initial rate of fluorescence calculated by best-fitting the recovery time to a mono-exponential curve, and calculating the initial gradient at the moment of bleaching. Gradient $f_{cell} - f_{surround}$ is measured experimentally; in fact, it is set by the protocol to be numerically 0.5 because the central cell is bleached until fluorescence decreases to 50%.

An accurate calculation of ρ would require volume rendering. However, it can be approximated by a reasonable assumption that the monolayer is cuboidal and contracts are made at the sides of cells (and not above or below the x-y plane). The monolayer image provides information about the area of the cell in the x-y plane, and its perimeter than makes contact with neighbouring cells. The cell's volume is thus area times height, and the cell's surface (at which it contacts are made) is the cell's perimeter times height. Thus, for the bleached cell,

$$\rho = \text{perimeter x height / area x height} = \text{perimeter/area}.$$

All these values are inferred from the data. The permeability refers specifically to calcein.

2. CALCULATING COUPLING COEFFICIENT FROM CELLTRACKER CO-CULTURES:

Monolayers are imaged sequentially to obtain violet and orange fluorescence bitmaps (512 by 512 pixels) at the optimal wavelength settings for CellTracker Violet and Orange respectively. Each experiment consistent of three conditions: (i) cells that were loaded with Violet only, (ii) cells that were loaded with Orange only, and (iii) a co-culture of cells that had been loaded with Violet or Orange, mixed in 1:1 ratio. Thus, (i) and (ii) are a monoculture, whereas (ii) is expected to be a well-mixed co-culture. Diffusive exchange across gap junctions is expected to lead to mixing of dyes between cells. This will have no effect on the mono-cultures as like is exchanged for like, but in co-cultures, some cells would contain Violet and Orange pixels. The degree of dye mixing was calculated by relating the violet and orange signal on a pixel-by-pixel basis. To ensure accuracy, several image processing steps are necessary.

Violet monoculture image processing:

1. In the violet fluorescence image:
   a. Background pixels are identified by thresholding. This is used to estimate confluency and the inverse to identify cells.
   b. The signal in non-background pixels is averaged to give a mean violet fluorescence value in cells. This is then used for normalizing the degree of violet dye loading, which may be different to the orange signal. This is called F_V^{mono}.
2. In the paired orange fluorescence image, the 95% percentile of signal in non-background pixels is calculated to describe background orange fluorescence. This represents autofluorescence in the orange range in the absence of CellTracker Orange. This value is called B_O^{mono}.
3. The process is repeated for all images taken in the same back (biological replicate) to obtain a mean F_V^{mono} and B_O^{mono}.

Orange monoculture image processing:

1. In the orange fluorescence image:
   a. Background pixels are identified by thresholding. This is used to estimate confluency and the inverse to identify cells.
   b. The signal in non-background pixels is averaged to give a mean orange fluorescence value in cells. This is then used for normalizing the degree of orange dye loading, which may be different to the violet signal. This is called F_O^{mono}.
2. In the paired violet fluorescence image, the 95% percentile of signal in non-background pixels is calculated to describe background violet fluorescence. This represents autofluorescence in the violet range in the absence of CellTracker Orange. This value is called B_V^{mono}. Typically, B_V^{mono} is larger than B_O^{mono}.
3. The process is repeated for all images taken in the same back (biological replicate) to obtain a mean F_O^{mono} and B_V^{mono}.

Once complete, means F_V^{mono} is background-subtracted by B_V^{mono}, and similarly for orange.

Co-culture image processing:

1. Background pixels are identified as those that are below the threshold for violet and orange fluorescence.
2. The non-background pixels are taken as areas within cells. Each pixel is annotated with a violet and orange fluorescence. These signals are background-subtracted (B_V^{mono} and B_O^{mono}, respectively), and then normalized to mean signals (F_V^{mono} and F_O^{mono}, respectively). Each pixel is now described by a background-subtracted and normalized fluorescence array, F_V and F_O.
3. To quantify exchange, violet fluorescence is expressed as a fraction of total fluorescence (F_V+F_O) and, similarly, orange fluorescence is expressed as a fraction of total fluorescence (F_V+F_O). The smaller of the two values is taken to represent coupling coefficient, as the smaller value relates to fluorescence from the ingress of CellTracker dye from neighboring cells, rather than dye that had been loaded originally in the cell. To scale this coefficient on a scale from 0 to 1, the final value is doubled.

FIGURE 1

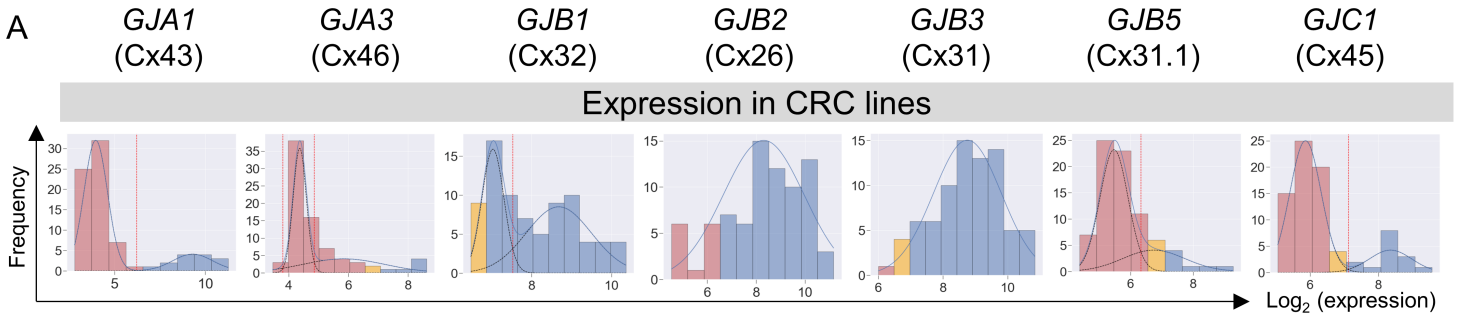
A
GJA1 (Cx43)
GJA3 (Cx46)
GJB1 (Cx32)
GJB2 (Cx26)
GJB3 (Cx31)
GJB5 (Cx31.1)
GJC1 (Cx45)
Expression in CRC lines
Frequency
Log2 (expression)

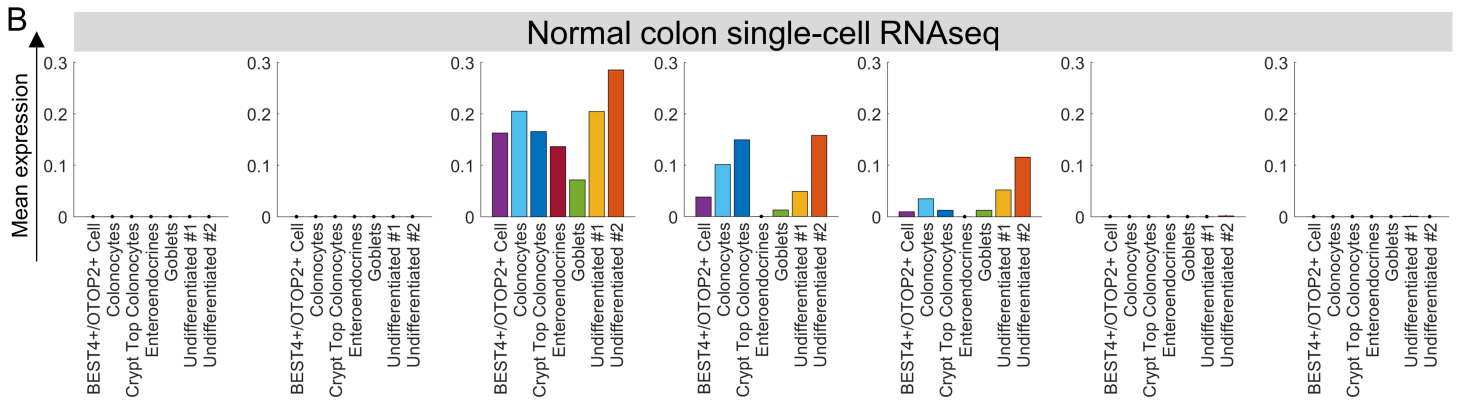
B
Normal colon single-cell RNAseq
Mean expression
BEST4+/OTOP2+ Cell
Colonocytes
Crypt Top Colonocytes
Enteroendocrines
Goblets
Undifferentiated #1
Undifferentiated #2

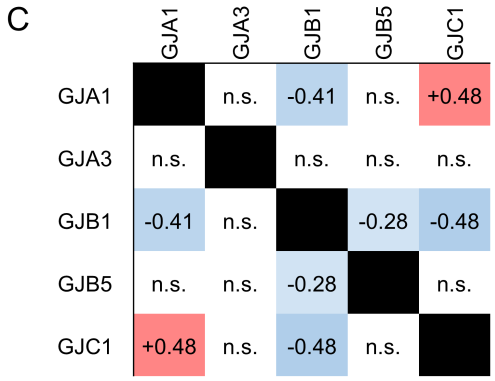
C
GJA1
GJA3
GJB1
GJB5
GJC1
n.s.
-0.41
+0.48
-0.28
-0.48

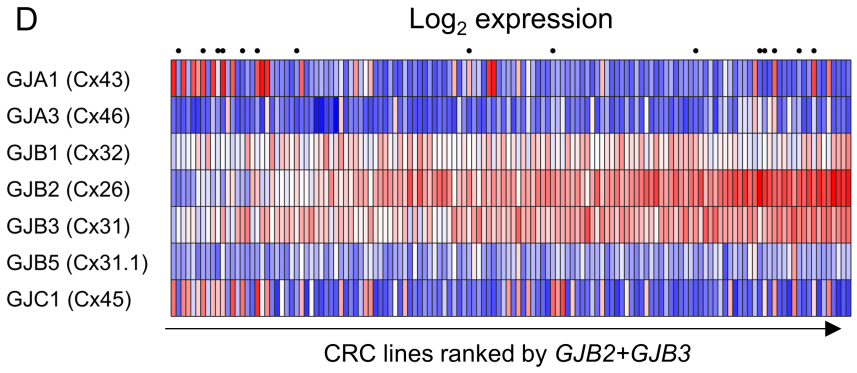
D
Log2 expression
GJA1 (Cx43)
GJA3 (Cx46)
GJB1 (Cx32)
GJB2 (Cx26)
GJB3 (Cx31)
GJB5 (Cx31.1)
GJC1 (Cx45)
CRC lines ranked by GJB2+GJB3

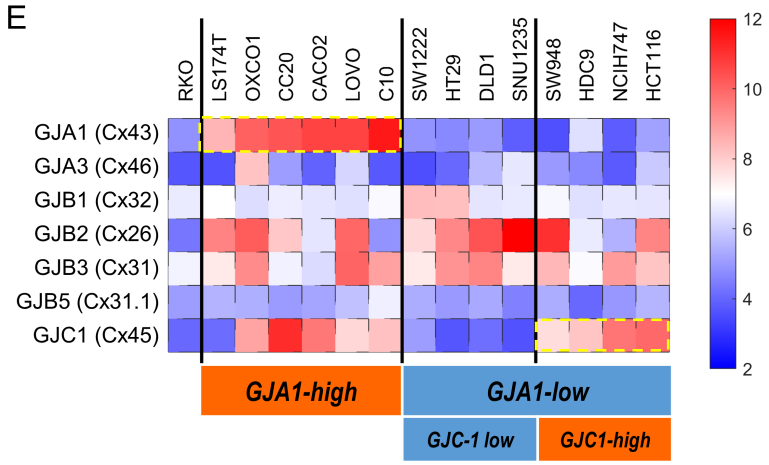
E
RKO
LS174T
OXCO1
CC20
CACO2
LOVO
C10
SW1222
HT29
DLD1
SNU1235
SW948
HDC9
NCIH747
HCT116
GJA1 (Cx43)
GJA3 (Cx46)
GJB1 (Cx32)
GJB2 (Cx26)
GJB3 (Cx31)
GJB5 (Cx31.1)
GJC1 (Cx45)
GJA1-high
GJA1-low
GJC-1 low
GJC1-high

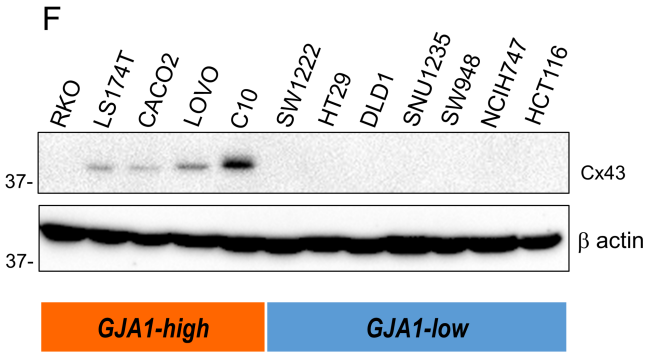
F
RKO
LS174T
CACO2
LOVO
C10
SW1222
HT29
DLD1
SNU1235
SW948
NCIH747
HCT116
37-
Cx43
β actin
GJA1-high
GJA1-low

FIGURE 2

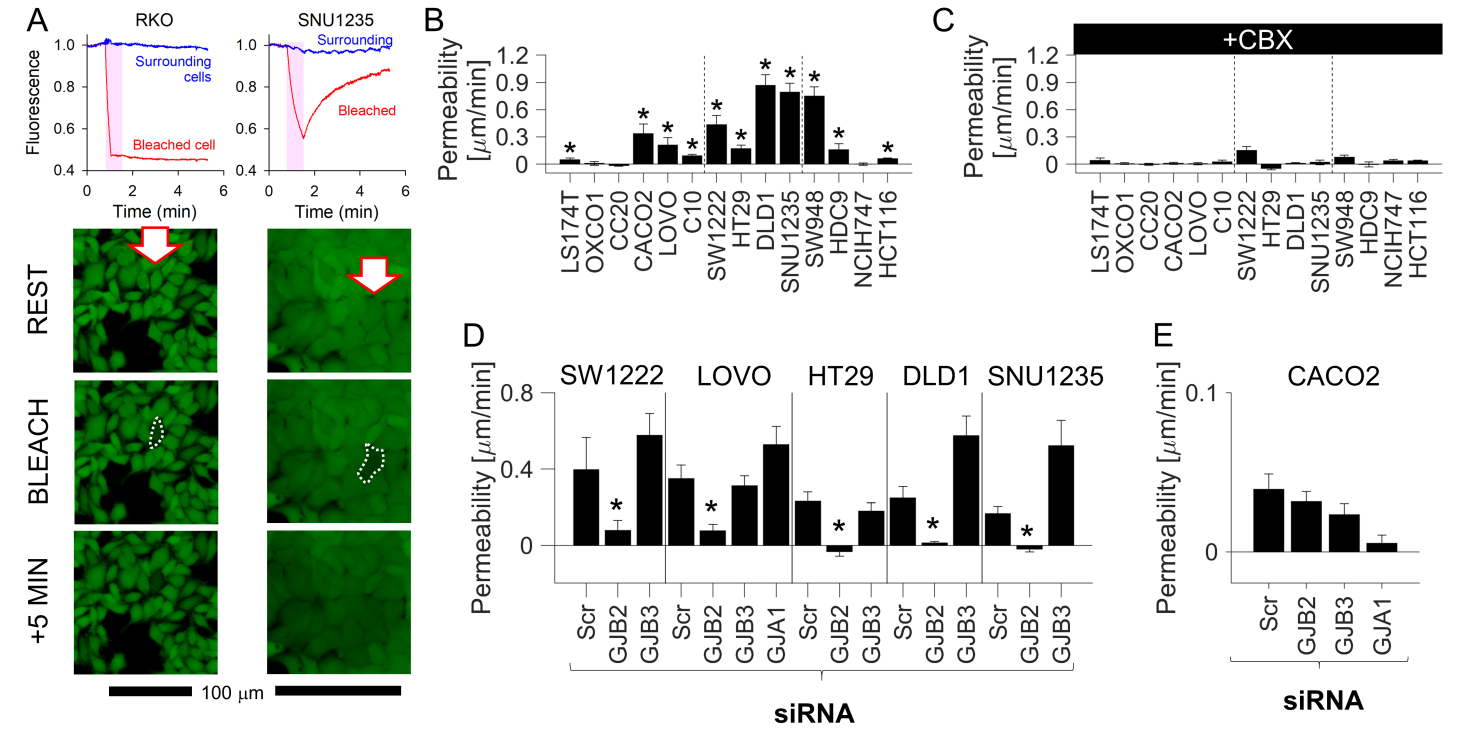
A
RKO
SNU1235
Surrounding
Surrounding cells
Bleached cell
Bleached
Fluorescence
Time (min)
REST
BLEACH
+5 MIN
100 µm
B
Permeability [µm/min]
LS174T
OXCO1
CC20
CACO2
LOVO
C10
SW1222
HT29
DLD1
SNU1235
SW948
HDC9
NCIH747
HCT116
C
+CBX
D
SW1222
LOVO
HT29
DLD1
SNU1235
Scr
GJB2
GJB3
GJA1
siRNA
E
CACO2
F
Cx26
RKO
C10
SW1222
HT29
HCT116
LS174T
LOVO
DLD1
SW948
SNU1235
G
Cx43
100 µm
H
Sorting by Cx43:
LOVO
Caco2
Cx43
β actin
I
SW1222
DLD1
WT
sgGJB2
Scramble
siGJB2
Cx26
GAPDH
J
SW1222 Scramble
SW1222 siGJB2
100 µm
K
DLD1
WT
KO1
KO2
KO3
Cx26
GAPDH
DLD1 WT
DLD1 KO1
50 µm
L
Calcein fluorescence
Surrounding cells
WT
KO1
Bleached cell
Time (s)
Permeability (µm/min)
***
WT
KO1
KO2
WT+CBX

FIGURE 3

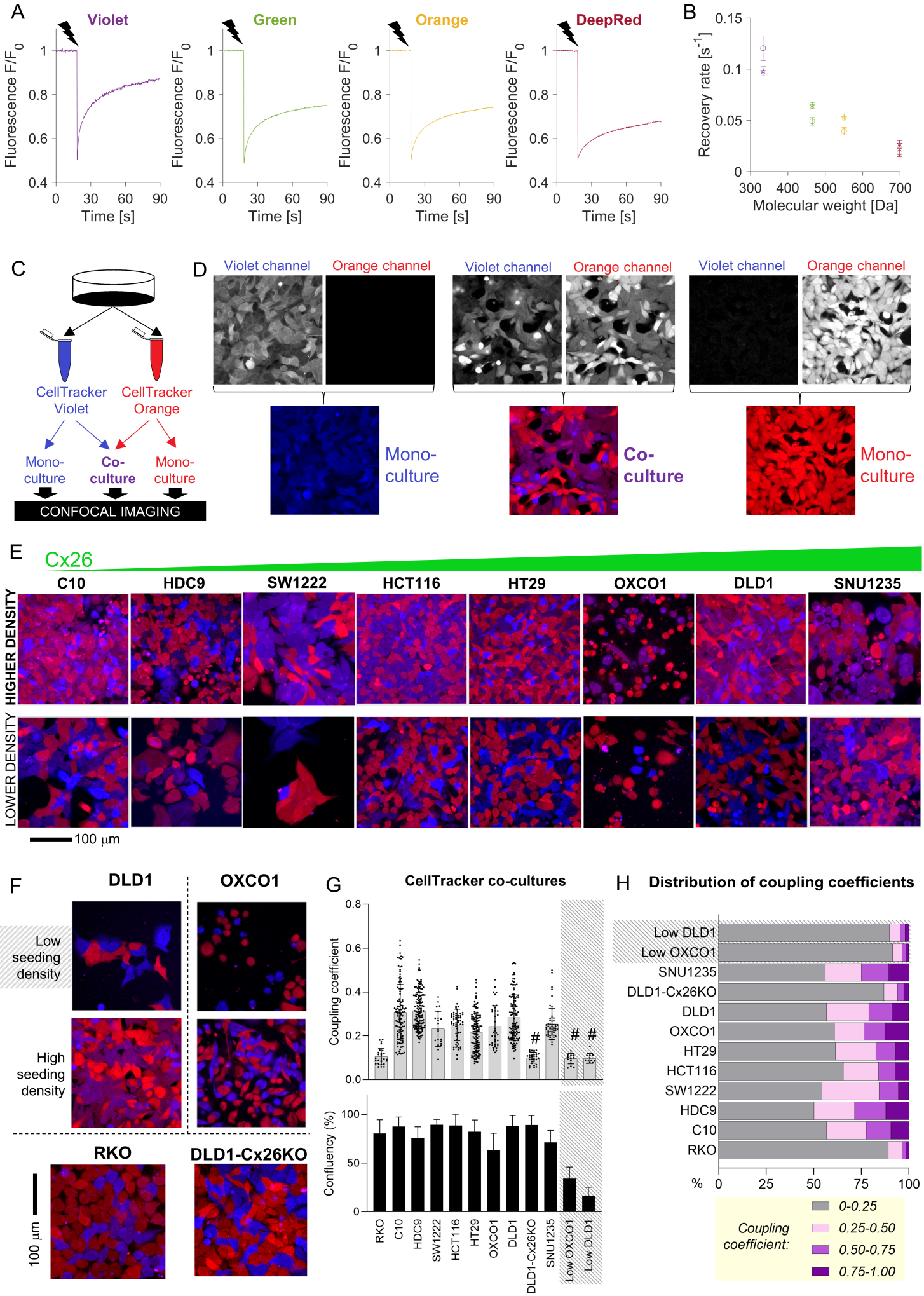
A
Violet
Green
Orange
DeepRed
Fluorescence F/F0
Time [s]
B
Recovery rate [s-1]
Molecular weight [Da]
C
CellTracker Violet
CellTracker Orange
Mono-culture
Co-culture
Mono-culture
CONFOCAL IMAGING
D
Violet channel
Orange channel
Mono-culture
Co-culture
Mono-culture
E
Cx26
C10
HDC9
SW1222
HCT116
HT29
OXCO1
DLD1
SNU1235
HIGHER DENSITY
LOWER DENSITY
100 µm
F
DLD1
OXCO1
Low seeding density
High seeding density
RKO
DLD1-Cx26KO
100 µm
G
CellTracker co-cultures
Coupling coefficient
Confluency (%)
RKO
C10
HDC9
SW1222
HCT116
HT29
OXCO1
DLD1
DLD1-Cx26KO
SNU1235
Low OXCO1
Low DLD1
H
Distribution of coupling coefficients
Low DLD1
Low OXCO1
SNU1235
DLD1-Cx26KO
DLD1
OXCO1
HT29
HCT116
SW1222
HDC9
C10
RKO
%
Coupling coefficient:
0-0.25
0.25-0.50
0.50-0.75
0.75-1.00

FIGURE 4

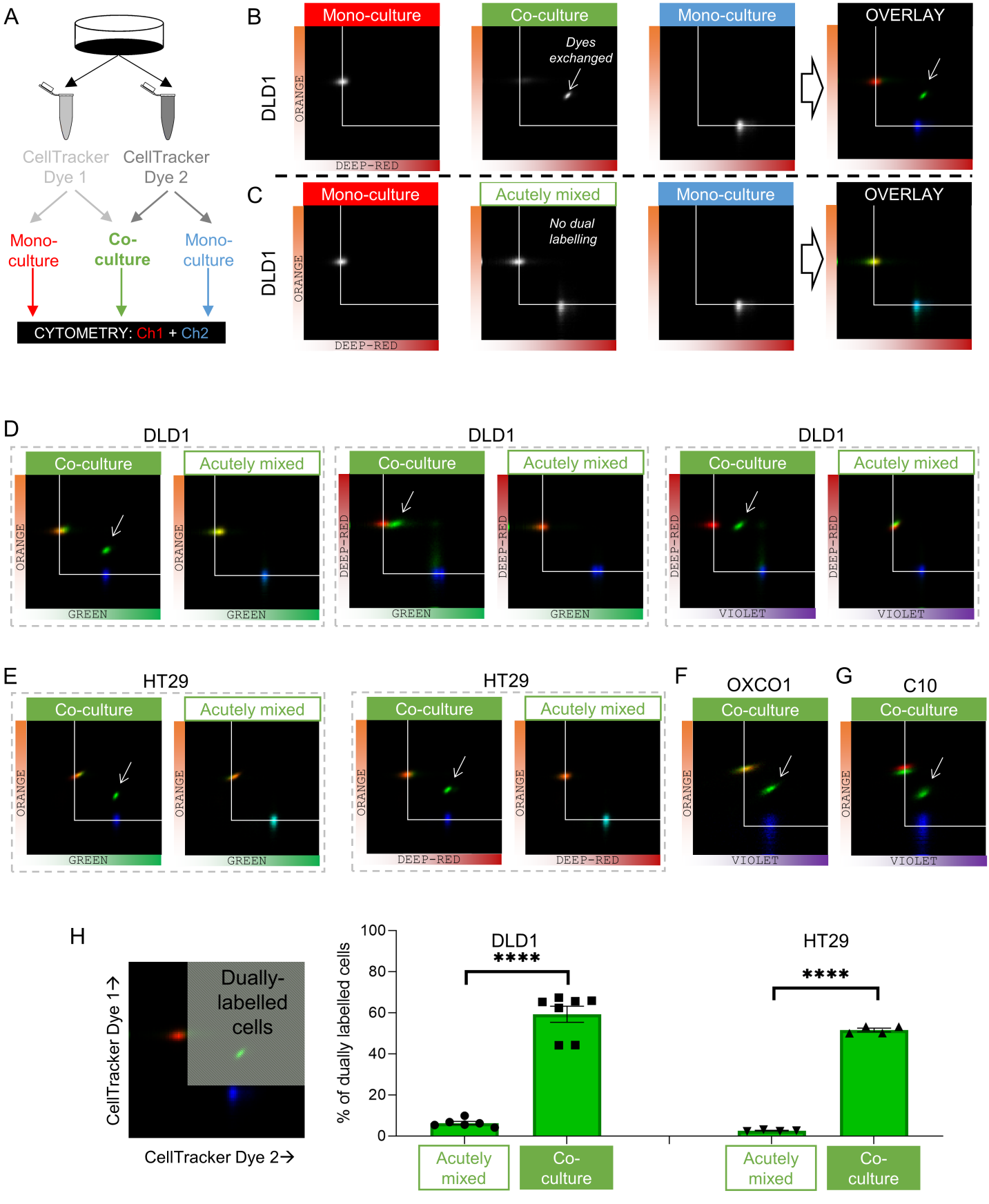
A
CellTracker Dye 1
CellTracker Dye 2
Mono-culture
Co-culture
Mono-culture
CYTOMETRY: Ch1 + Ch2
B
Mono-culture
Co-culture
Mono-culture
OVERLAY
DLD1
Dyes exchanged
ORANGE
DEEP-RED
C
Mono-culture
Acutely mixed
Mono-culture
OVERLAY
DLD1
No dual labelling
ORANGE
DEEP-RED
D
DLD1
DLD1
DLD1
Co-culture
Acutely mixed
ORANGE
GREEN
DEEP-RED
VIOLET
E
HT29
HT29
F
OXCO1
G
C10
H
Dually-labelled cells
CellTracker Dye 1→
CellTracker Dye 2→
% of dually labelled cells
100
80
60
40
20
0
DLD1
HT29
****
Acutely mixed
Co-culture

FIGURE 5

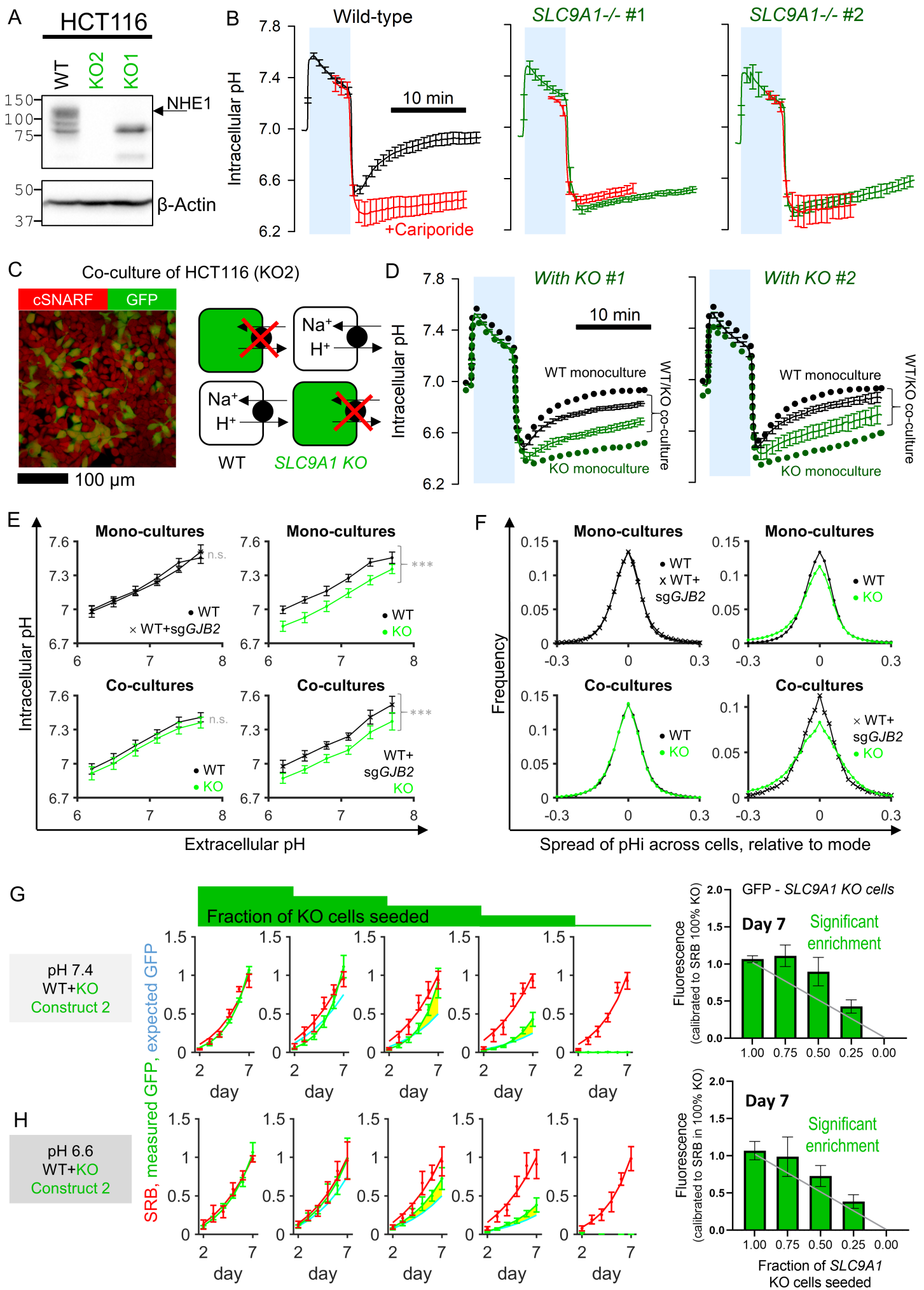
A
HCT116
WT
KO2
KO1
150
100
75
NHE1
50
37
β-Actin
B
Wild-type
SLC9A1-/- #1
SLC9A1-/- #2
Intracellular pH
7.8
7.4
7.0
6.6
6.2
10 min
+Cariporide
C
Co-culture of HCT116 (KO2)
cSNARF
GFP
100 µm
Na+
H+
WT
SLC9A1 KO
D
With KO #1
With KO #2
10 min
WT monoculture
KO monoculture
WT/KO co-culture
E
Mono-cultures
Co-cultures
n.s.
***
WT
WT+sgGJB2
KO
Intracellular pH
Extracellular pH
F
Frequency
Spread of pHi across cells, relative to mode
G
Fraction of KO cells seeded
pH 7.4
WT+KO
Construct 2
SRB, measured GFP, expected GFP
day
GFP - SLC9A1 KO cells
Day 7
Significant enrichment
Fluorescence (calibrated to SRB 100% KO)
1.00 0.75 0.50 0.25 0.00
H
pH 6.6
WT+KO
Construct 2
Fraction of SLC9A1 KO cells seeded

FIGURE 6

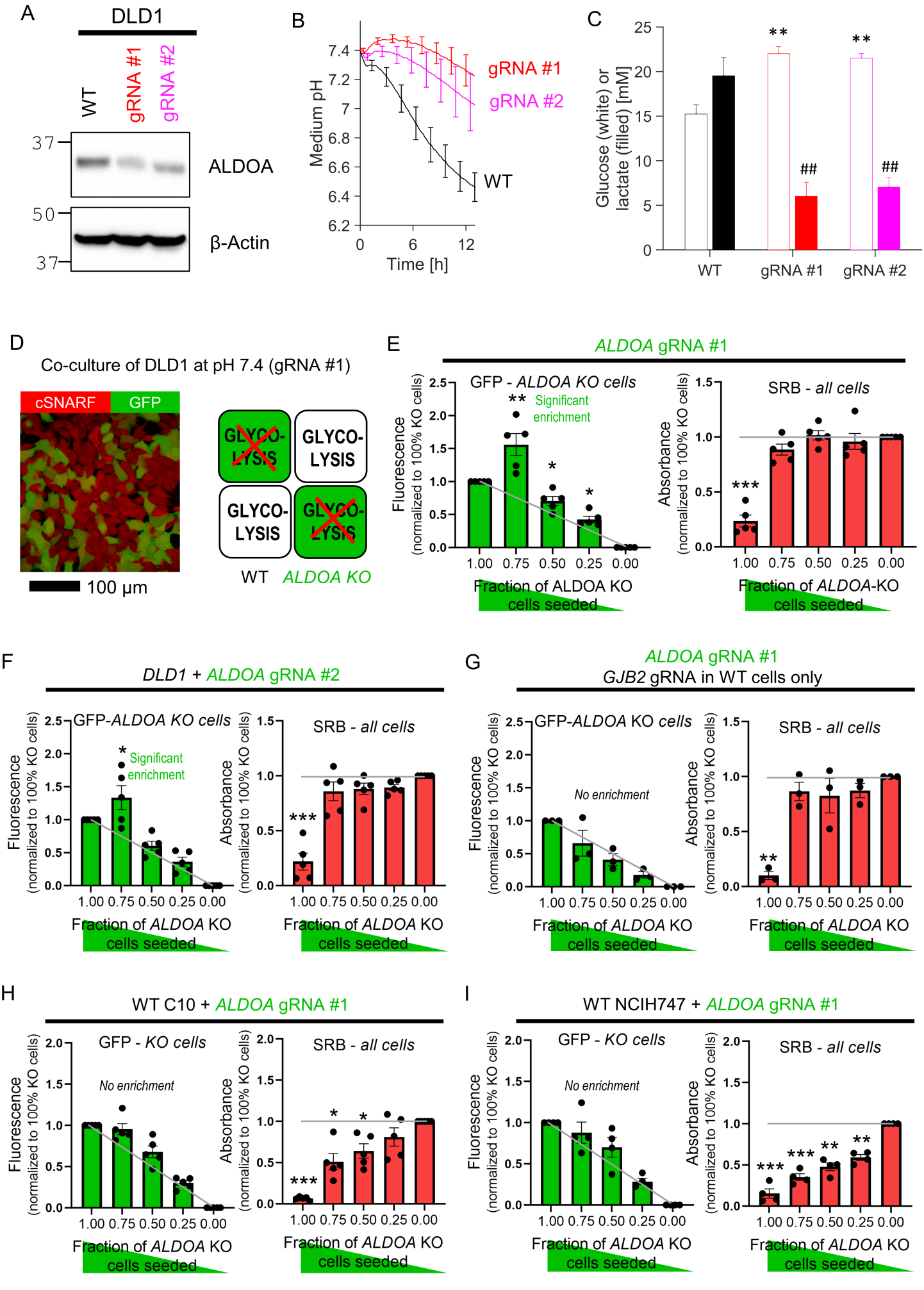
A
DLD1
WT
gRNA #1
gRNA #2
37
ALDOA
50
β-Actin
37
B
Medium pH
7.4
7.2
7
6.8
6.6
6.4
6.2
0
6
12
Time [h]
gRNA #1
gRNA #2
WT
C
Glucose (white) or lactate (filled) [mM]
25
20
15
10
5
0
**
**
##
##
WT
gRNA #1
gRNA #2
D
Co-culture of DLD1 at pH 7.4 (gRNA #1)
cSNARF
GFP
100 µm
GLYCO-LYSIS
GLYCO-LYSIS
GLYCO-LYSIS
GLYCO-LYSIS
WT
ALDOA KO
E
ALDOA gRNA #1
GFP - ALDOA KO cells
Fluorescence (normalized to 100% KO cells)
** Significant enrichment
*
*
1.00 0.75 0.50 0.25 0.00
Fraction of ALDOA KO cells seeded
SRB - all cells
Absorbance (normalized to 100% KO cells)
***
1.00 0.75 0.50 0.25 0.00
Fraction of ALDOA-KO cells seeded
F
DLD1 + ALDOA gRNA #2
GFP-ALDOA KO cells
Fluorescence (normalized to 100% KO cells)
* Significant enrichment
1.00 0.75 0.50 0.25 0.00
Fraction of ALDOA KO cells seeded
SRB - all cells
Absorbance (normalized to 100% KO cells)
***
1.00 0.75 0.50 0.25 0.00
Fraction of ALDOA KO cells seeded
G
ALDOA gRNA #1
GJB2 gRNA in WT cells only
GFP-ALDOA KO cells
Fluorescence (normalized to 100% KO cells)
No enrichment
1.00 0.75 0.50 0.25 0.00
Fraction of ALDOA KO cells seeded
SRB - all cells
Absorbance (normalized to 100% KO cells)
**
1.00 0.75 0.50 0.25 0.00
Fraction of ALDOA KO cells seeded
H
WT C10 + ALDOA gRNA #1
GFP - KO cells
Fluorescence (normalized to 100% KO cells)
No enrichment
1.00 0.75 0.50 0.25 0.00
Fraction of ALDOA KO cells seeded
SRB - all cells
Absorbance (normalized to 100% KO cells)
*
*
***
1.00 0.75 0.50 0.25 0.00
Fraction of ALDOA KO cells seeded
I
WT NCIH747 + ALDOA gRNA #1
GFP - KO cells
Fluorescence (normalized to 100% KO cells)
No enrichment
1.00 0.75 0.50 0.25 0.00
Fraction of ALDOA KO cells seeded
SRB - all cells
Absorbance (normalized to 100% KO cells)
***
***
**
**
1.00 0.75 0.50 0.25 0.00
Fraction of ALDOA KO cells seeded

FIGURE 7

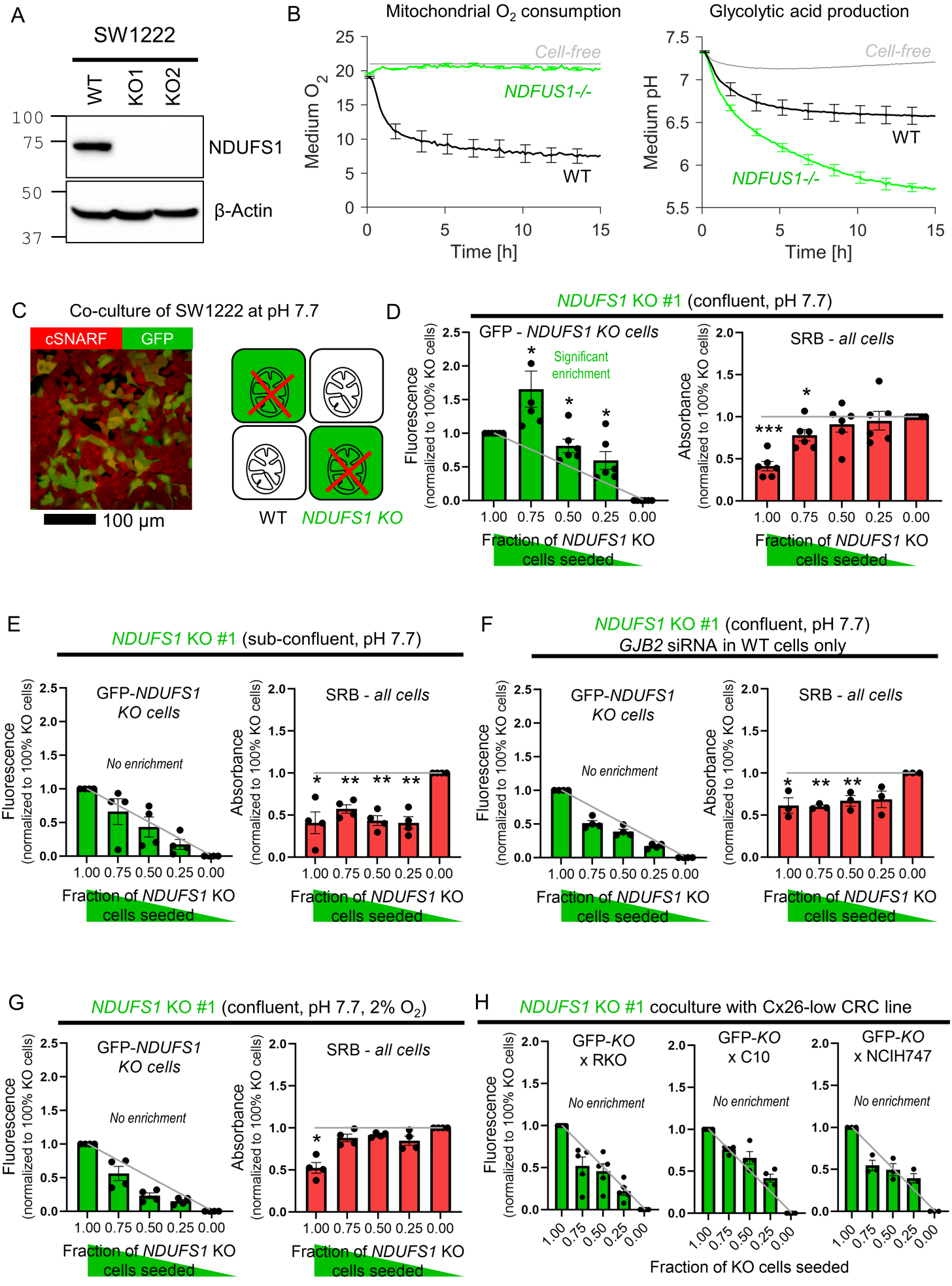
A
SW1222
WT
KO1
KO2
100
75
NDUFS1
50
β-Actin
37
B
Mitochondrial O_2 consumption
Medium O_2
Cell-free
NDFUS1-/-
WT
Time [h]
Glycolytic acid production
Medium pH
Cell-free
WT
NDFUS1-/-
Time [h]
C
Co-culture of SW1222 at pH 7.7
cSNARF
GFP
100 µm
WT
NDUFS1 KO
D
NDUFS1 KO #1 (confluent, pH 7.7)
GFP - NDUFS1 KO cells
Significant enrichment
Fluorescence (normalized to 100% KO cells)
Fraction of NDUFS1 KO cells seeded
SRB - all cells
Absorbance (normalized to 100% KO cells)
Fraction of NDUFS1 KO cells seeded
E
NDUFS1 KO #1 (sub-confluent, pH 7.7)
GFP-NDUFS1 KO cells
No enrichment
Fluorescence (normalized to 100% KO cells)
Fraction of NDUFS1 KO cells seeded
SRB - all cells
Absorbance (normalized to 100% KO cells)
Fraction of NDUFS1 KO cells seeded
F
NDUFS1 KO #1 (confluent, pH 7.7)
GJB2 siRNA in WT cells only
GFP-NDUFS1 KO cells
No enrichment
Fluorescence (normalized to 100% KO cells)
Fraction of NDUFS1 KO cells seeded
SRB - all cells
Absorbance (normalized to 100% KO cells)
Fraction of NDUFS1 KO cells seeded
G
NDUFS1 KO #1 (confluent, pH 7.7, 2% O_2)
GFP-NDUFS1 KO cells
No enrichment
Fluorescence (normalized to 100% KO cells)
Fraction of NDUFS1 KO cells seeded
SRB - all cells
Absorbance (normalized to 100% KO cells)
Fraction of NDUFS1 KO cells seeded
H
NDUFS1 KO #1 coculture with Cx26-low CRC line
GFP-KO x RKO
GFP-KO x C10
GFP-KO x NCIH747
No enrichment
Fluorescence (normalized to 100% KO cells)
Fraction of KO cells seeded

FIGURE 8

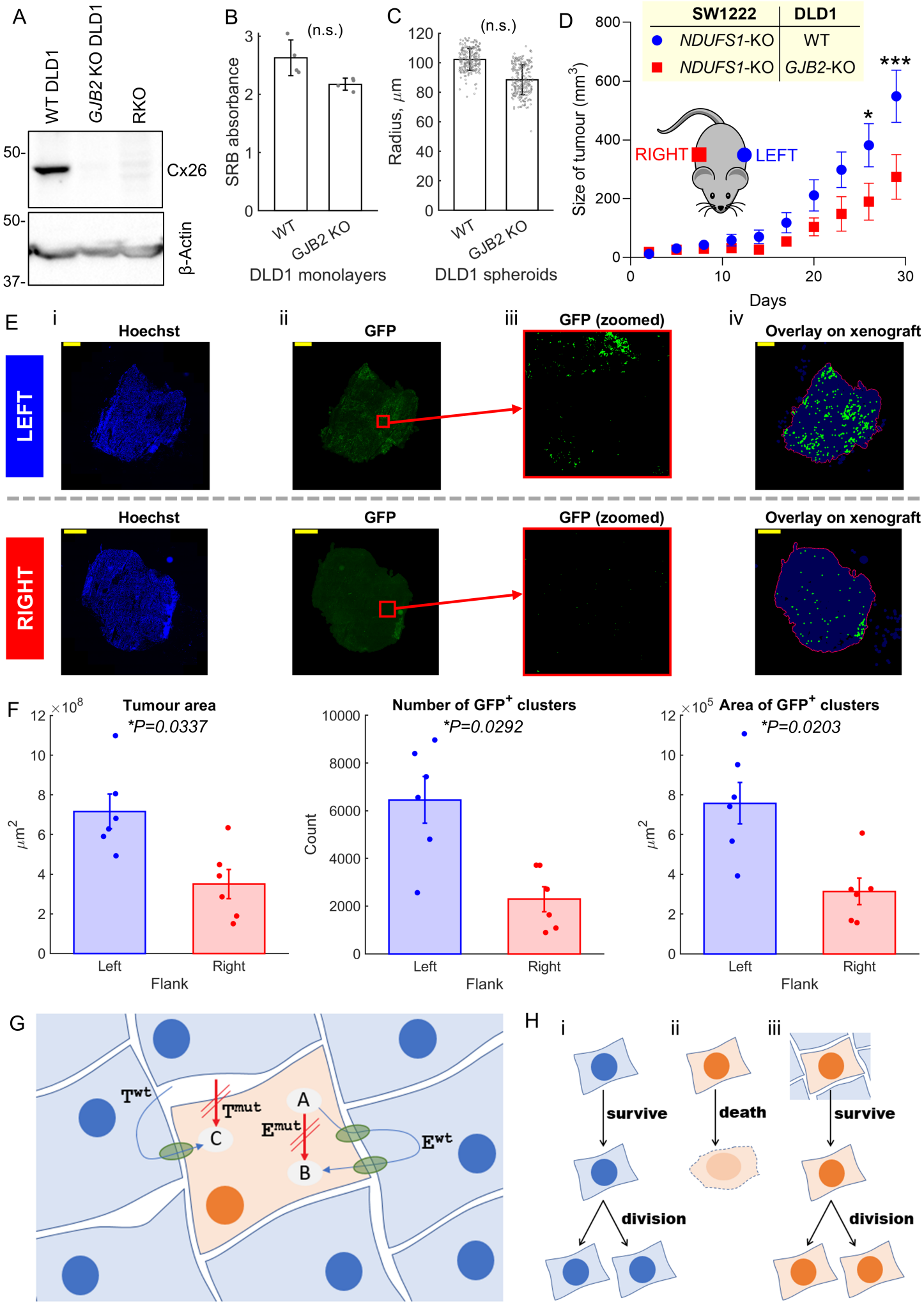
A
WT DLD1
GJB2 KO DLD1
RKO
50-
Cx26
50-
β-Actin
37-
B
(n.s.)
SRB absorbance
WT
GJB2 KO
DLD1 monolayers
C
(n.s.)
Radius, μm
WT
GJB2 KO
DLD1 spheroids
D
SW1222
DLD1
NDUFS1-KO
WT
NDUFS1-KO
GJB2-KO
Size of tumour (mm3)
RIGHT
LEFT
*
***
Days
E
i
Hoechst
ii
GFP
iii
GFP (zoomed)
iv
Overlay on xenograft
LEFT
RIGHT
F
Tumour area
*P=0.0337
μm2
Number of GFP+ clusters
*P=0.0292
Count
Area of GFP+ clusters
*P=0.0203
μm2
Left
Right
Flank
G
Twt
Tmut
Emut
Ewt
A
B
C
H
i
ii
iii
survive
death
survive
division
division

FIGURE 1-figure supplement 1

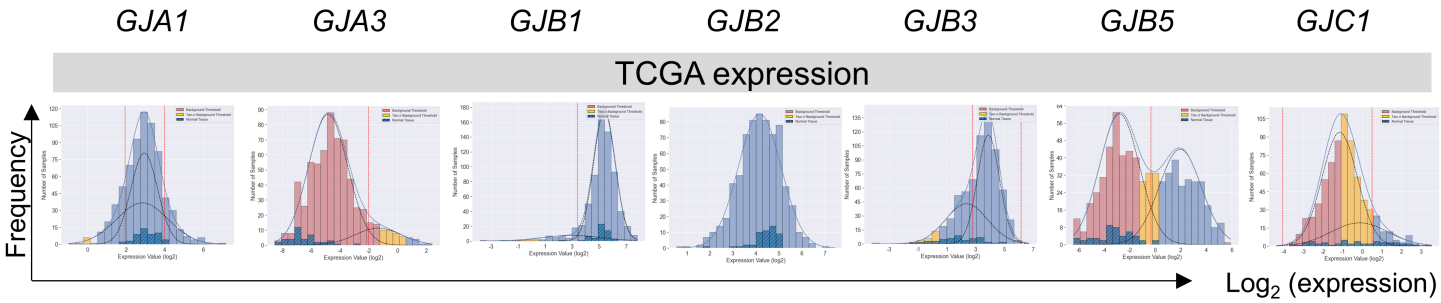

FIGURE 1-figure supplement 2

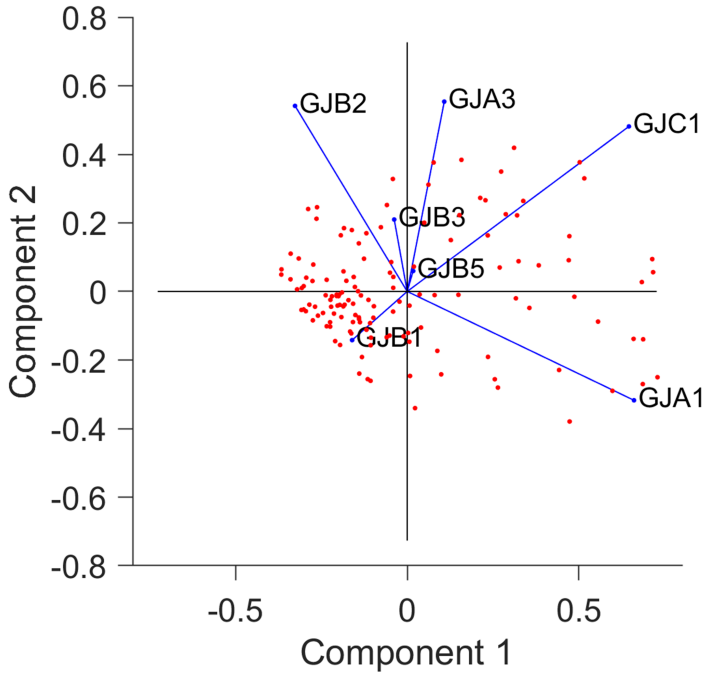

FIGURE 2-figure supplement 1

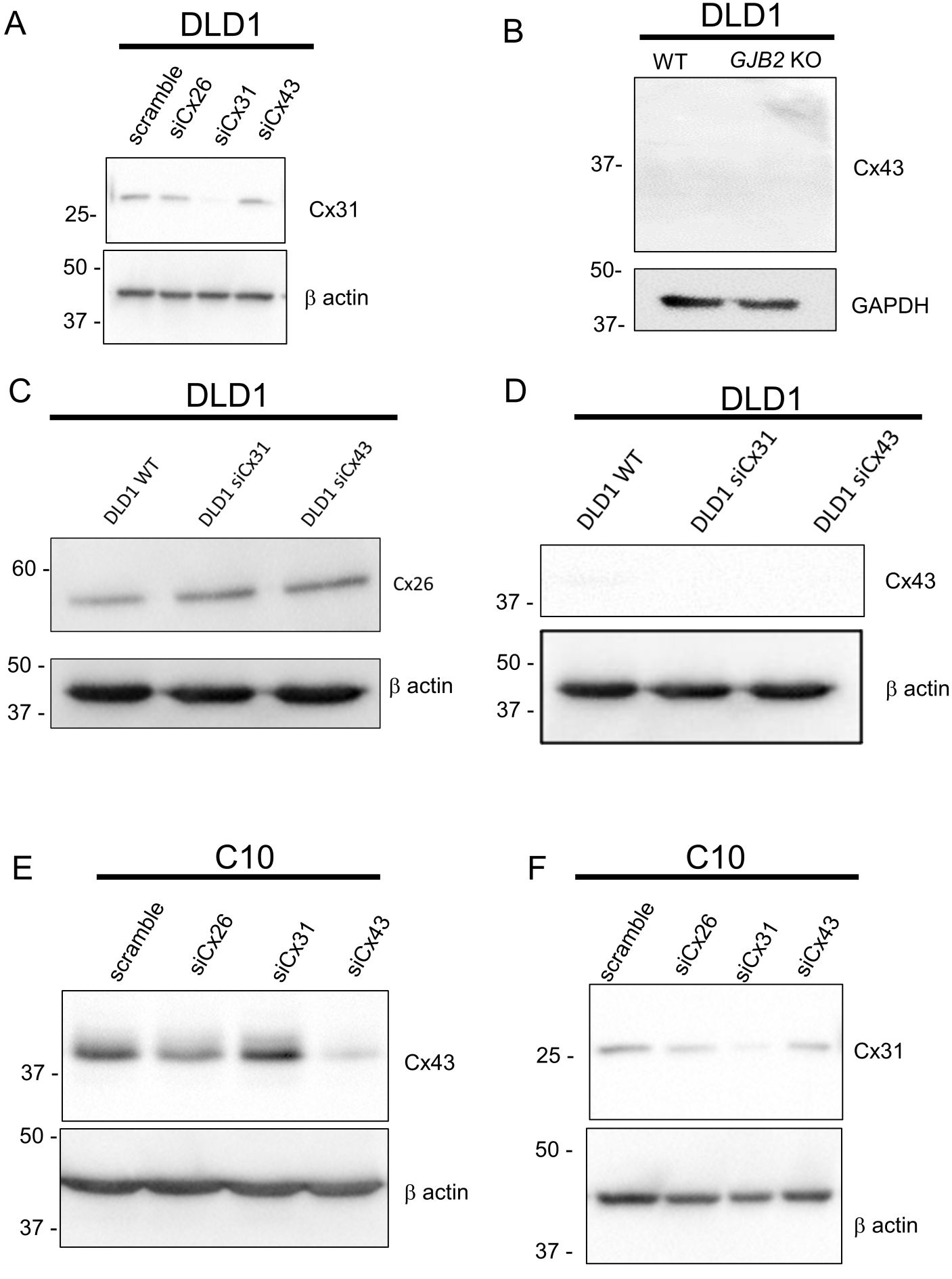

FIGURE 2-figure supplement 2

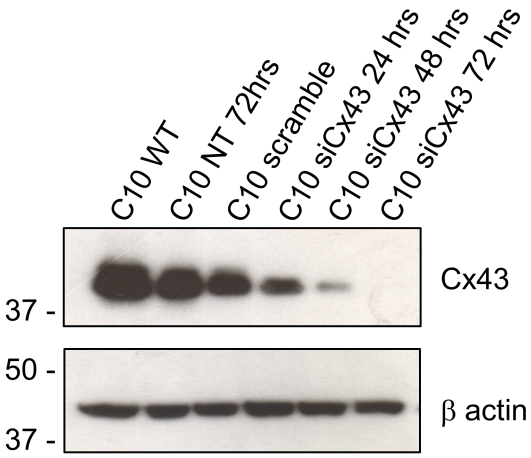

FIGURE 3-figure supplement 1

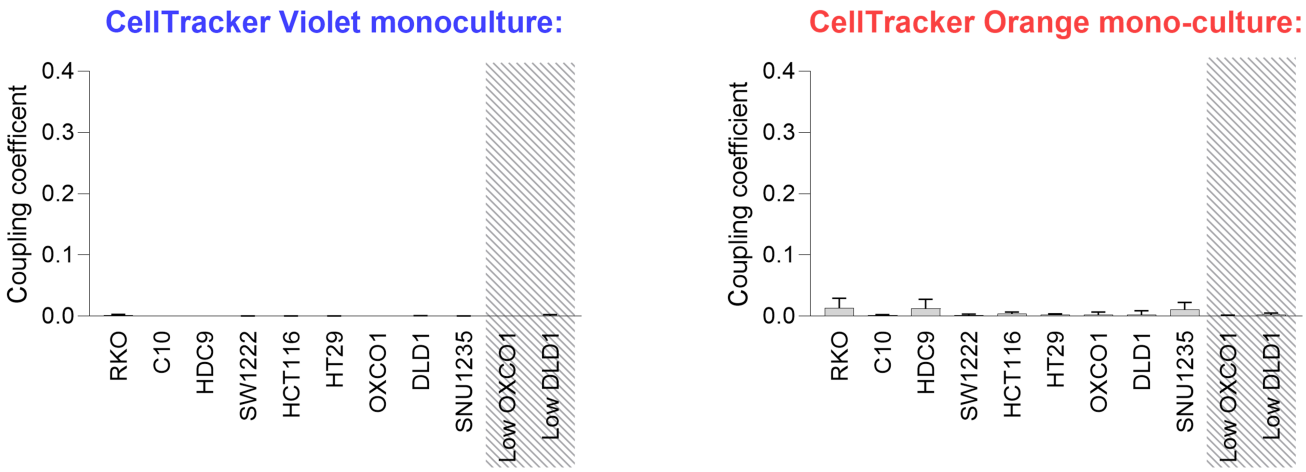

FIGURE 5-figure supplement 1

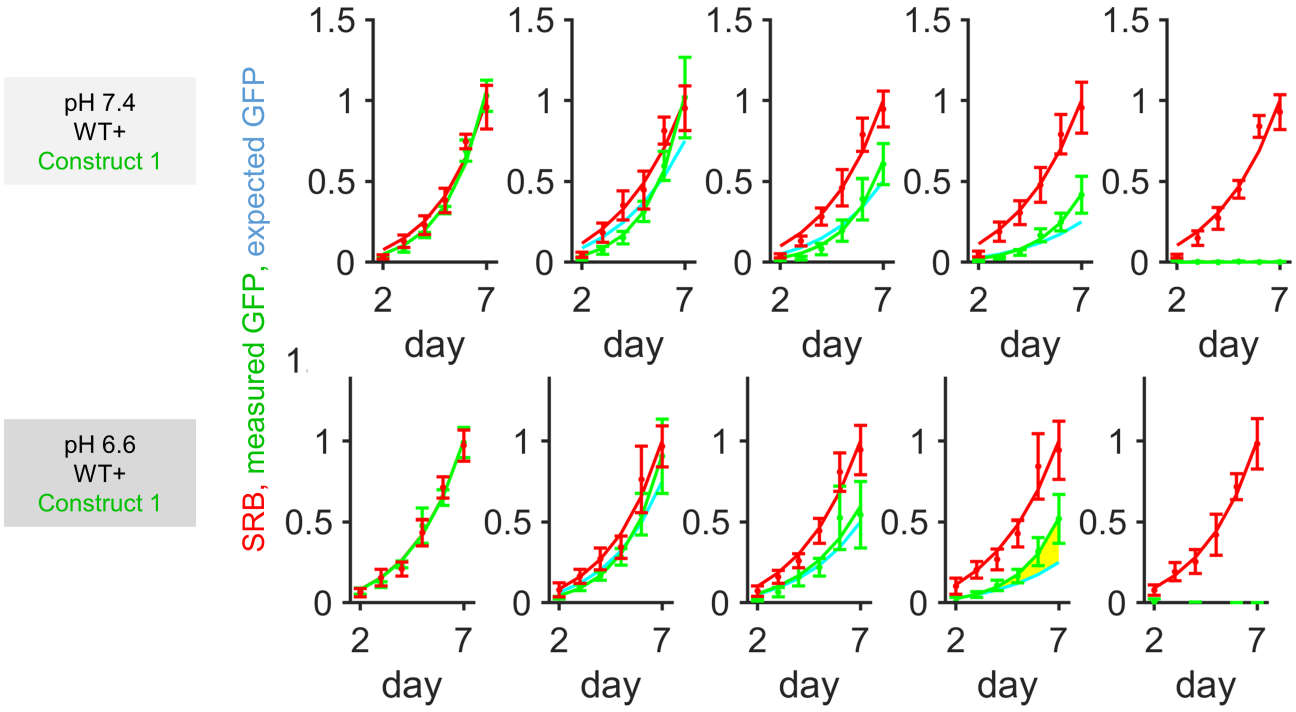

FIGURE 6-figure supplement 1

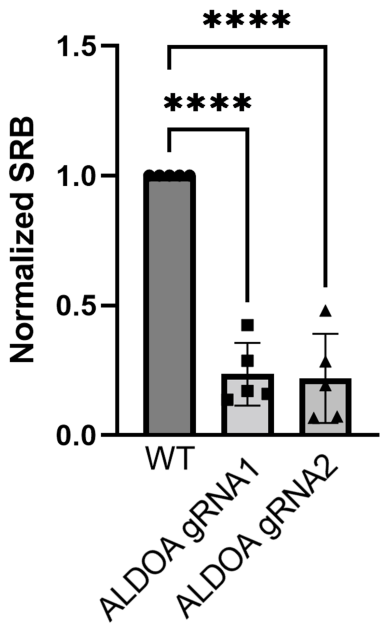

FIGURE 6-figure supplement 2

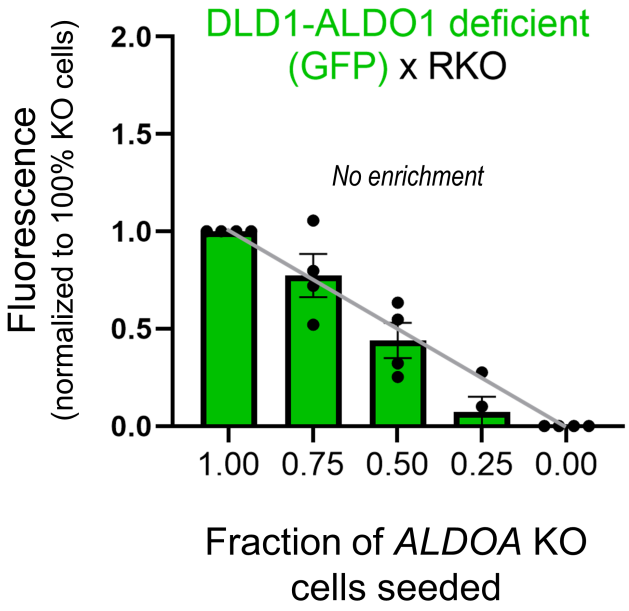

FIGURE 6-figure supplement 3

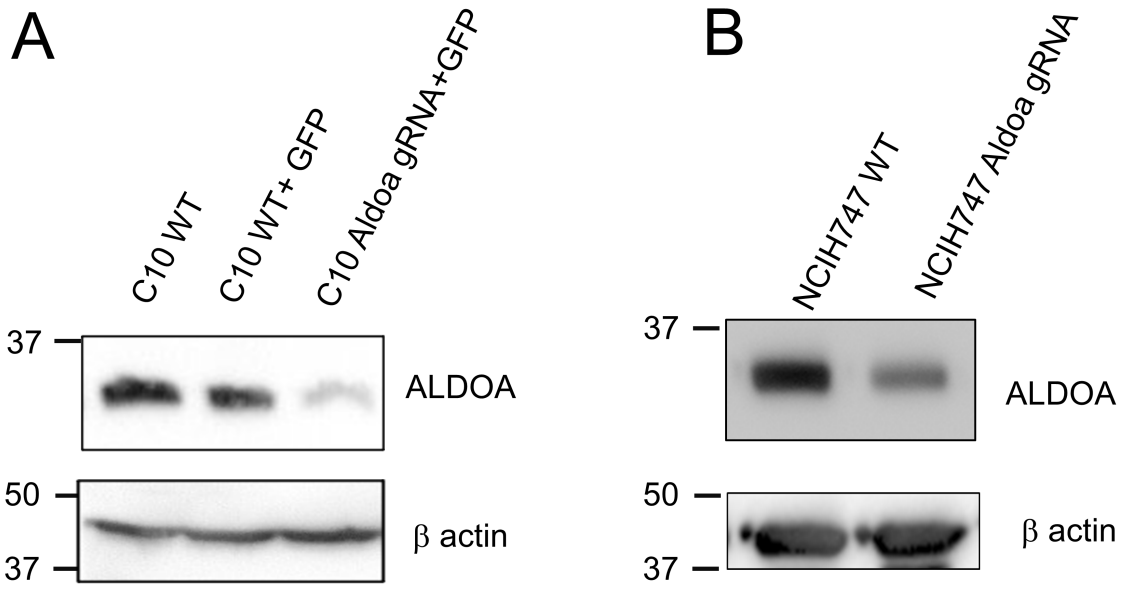

FIGURE 7-figure supplement 1

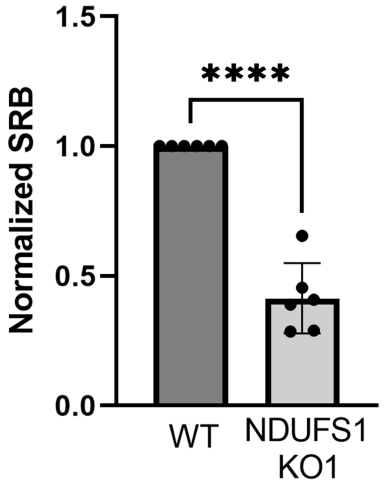

FIGURE 8-figure supplement 1